

The authors wish to thank the referees and Dr. van Dienenhoven for their comments and suggestions. Below, we respond to each of the remarks. The comments are displayed in quotes, with our responses **bolded**.

1 Anonymous Referee #1

“General comments This article presents a detailed analysis and study of the effects of different kinds of internal inhomogeneity on the light scattering properties of atmospheric aerosol. The authors provide a detailed account of how they analysed the aerosol internal structure and geometrically modeled the particles. They employ the DDA method to study the resulting light scattering behaviours assuming different kinds of aerosol inhomogeneity, and these results are compared to an effective medium approximation. In general, they find that the chosen effective medium approximation to be inadequate in predicting the polarized and intensity-related elements of the scattering phase matrix. They conclude that to represent the light scattering properties of aerosol, the interior dielectric properties as well as their distributions throughout the particle volume should be taken into account explicitly. They also show that the effects of the internal inclusions on light scattering are not cancelled out when integral optical properties are considered such as ω_0 and g . These latter quantities are parameterized in climate models, and so one might be able to say, based on this paper, that current climate models are biased, as these naturally assume effective medium approximations to parameterize the integral optical properties. The conclusions of this paper are equally important for remote sensing studies of aerosol, as they use the angle-dependent quantities contained in the scattering phase matrix.”

We agree with the referee that our findings have implications both on climate modelling and remote sensing.

“It was a surprise to read that the authors did not explicitly advocate a greater use of polarization measurements to help identify aerosol types as their polarized matrix element figures suggest a distinct dependence of polarization on the particular case being considered. The authors should state this more distinctly, as this will help to promote more polarization measurements of atmospheric aerosol, especially from space.”

As the article was mainly a sensitive study of different internal structure effects, we did not focus on aerosol identification. However, we fully agree with the referee that for identifying the aerosol types, polarization measurements are greatly beneficial, especially because they provide additional, independent information that is sensitive to potential microphysical characteristics. We have added

text about this to the end of Sections 5.2. and 6.

“There are no objections to this paper being published, although there are comments below, which the authors should address before eventual full publication.”

We thank the referee of their assessment and reply to their comments individually below.

“1. The authors take great pains to stress the importance of internal inhomogeneities. My question is how important is surface roughness and might this be more prominent than inclusions or are they both as important as each other? The authors do not actually discuss surface roughness until the very end, and there they state that an opposite effect on the linear depolarization ratio is found. Is the effect only on that ratio or are the other matrix elements similarly affected? Please discuss.”

The impact of surface roughness is a very complicated topic, because the effects depend on both the particle properties but also on the roughness characteristics and the matrix element or other quantity being considered. A general treatment of surface roughness is beyond the focus of this work, but we have provided a few qualitative comparisons in the Summary section based on our earlier work on surface roughness of irregular dust particles.

“2. Only one effective medium approximation is compared against. Do the results in this paper hold for all effective medium approximations? For instance, if they were to assume the Maxwell-Garnett mixing rule, would it be true to say that this approximation provides better agreement with their exact calculations. Please discuss and show an example in reply.”

The question about using different effective-medium approximations was also pointed out in the short comment by Dr. van Diedenhoven. We will answer both of the concerns in Section 4 of this response, rather than spread the answer in two separate places.

“3. Is the error in the EMA, in calculating the integral optical properties, significant with respect to current experimental uncertainties? What are the current experimental uncertainties in determining ω_0 and g ? The effective medium approximation is within -6% of the exact calculations. Are the current experimental uncertainties now less than the at most -6% difference?”

Whether an error of -6% is significant depends on the quantity of interest and also on the situation. For example, an error of 6% in g may not be critical for the radiative effect of an optically thin aerosol layer. Then again, 6% error in albedo may correspond to a much larger relative error in the co-albedo, which may give rise to quite substantial effects in the absorptivity of the aerosol

layer. Whether such errors are measurable again depends on the quantity of interest and the measurement arrangement. Our understanding is that the impact of inhomogeneity may not be the dominant source of error in all cases, but nevertheless is often important and measurable if other sources of uncertainty can be accounted for properly.

“4. Was the aerosol shown in Figure 1 collected on the ground or when suspended in the atmosphere? If collected on the ground, then that aerosol may not necessarily be representative of the aerosol suspended in the atmosphere as it might have been modified? Please discuss possible aerosol modifications if picked up off the ground.”

Dust particles were collected directly from air on a borosilicate glass-fiber filter using a total suspended particulate (TSP) sampler. We have selected individual dust particles using scanning electron microscope, and then prepared thin cross-sectional slices from the particles with focused ion beam. Then, the slices were observed with transmission electron microscope to analyze internal structures and identify constituent minerals. We confirm that the internal structures obtained by above procedure are representative of those of dust particles in suspension. Full details are provided in Jeong and Nousiainen, TEM analysis of the internal structures and mineralogy of Asian dust particles and the implications for optical modeling, *Atmospheric Chemistry and Physics*, 14, 72337254, 2014, which is cited in Section 2.

“5. How might the differences presented in the light scattering figures change if the real PSDs were to change from say narrow to broad PSDs? Might there be some cancellation in error over a fully integrated PSD to obtain the volumetric aerosol optical properties? Please discuss.”

Errors that are random in nature would likely be cancelled or dampened due to integration over broader PSD, while errors that grow at larger size parameters would likely be amplified. For example, Case 5 polarization elements would likely have a larger error with a wider PSD due to larger size parameters having larger EMA errors than small size parameters. On the other hand, Case 2 errors might in fact get systematically smaller with a broad PSD. Random error averaging would probably play a larger role with very regular shapes where the scattering matrix elements oscillate more strongly than irregular shapes. We have added discussion about the effects of wider PSDs in Section 5.2.

“Minor Points 1. Citations. The following citation might also be deserving of inclusion in this paper. Short-wave and long-wave radiative properties

of Saharan dust aerosol. Osborne, S.R.; Baran, A.J.; Johnson, B.T.; Haywood, J.M.; Hesse, Evelyn; Newman, S. In: Quarterly Journal of the Royal Meteorological Society, Vol. 137, No. 658, 2011, p. 1149-1167.

We agree on the significance of the article and have included it.

2. The author list in Haywood et al. (2011) is incomplete. It should be as follows: Haywood, J. M., Johnson, B. T., Osborne, S. R., Baran, A. J., Brooks, M., Milton, S. F., Mulcahy, J., Walters, D., Allan, R. P., Klaver, A., Formenti, P., Brindley, H. E., Christopher, S. and Gupta, P.

The referee seems to be referring to another Haywood et al. (2011), doi:10.1002/qj.797 instead of doi:10.1002/qj.770 that this article cites. Regardless, it seems that the article in question is also relevant to the discussion and we have thus included it as well.

3. Introduction. Surface roughness is also an important contribution to the radiative properties of aerosol. Please discuss.

Surface roughness is now briefly mentioned in the Introduction, and is discussed in more detail in Summary as requested in the Referee's major point #1, above.

4. Page 4 line 7 coinciding → coincident

Done

5. Page 4 line 20 is perfectly true? As there are approximations in the model constructions.

We have changed the word "perfect" to "completely". The text was referring to the fact that the model parameters were known completely, not that the model represents the physical reality perfectly. 6. Section 2. Page 5. Line 9 "..in a" redundant → "transported long-range"

Done

7. Section 2. Page 5. Line 26. Do you mean to say that orientations are more common with coarser mineral inclusions? The current sentence is difficult to follow. Please re-write.

Clarified

8. Section 3. Page 6. Line 2. Potential to do what? Incomplete sentence.

Clarified

9. Section 3. Page 6. Line 11. "establish the population" with respect to what?

Clarified

10. Section 3. Page 7. Line 2. "with" → in

Done

11. Section 3. Page 7. Line 7. "where" → which

Done

12. Section 3. Page 8. Line 11. $S11=S22$, $\delta = 0$ is only true for a sin-

gle sphere, you use the word particles, which implies multiple scattering, in which case $\delta \neq 0$.

Clarified

13. Section 3. Page 7. Line 18. is the scattering angle, i.e.,

Done

14. Section 3. Page 9. Why 8192 orientations? Were solutions convergent with this number of orientations? Please state accuracy.

8192 is the number of orientations used by ADDA by default (2^{5+4+4}). Solutions were convergent. Further, DDA accuracy has been discussed in greater detail in our response to Dr. Yurkin's comments, below, and the DDA section in the article has been expanded.

15. Section 4. Page 10. Line 6. A useful measure of a particle model is comparison of its area ratio to measured area ratios. Are these available? Or can you obtain from the data? Area ratio is a ratio of cross sections, so obviously this ratio will be of importance in light scattering calculations.

Unfortunately, area ratios are not readily available, and it would be challenging to obtain them for this data. Moreover, the dust particles shown were not meant to be replicated perfectly by the model particles, and therefore we don't consider this kind of a comparison critical.

16. Section 5. Page 16. Line 7. By definition spheres are perfect unless otherwise stated.

Redundant perfect removed

17. Section 5. Page 17. Line 20. smoothened→smoothed

Done

18. Section 5. Page 17. Line 22. Why not compare your results against the Amsterdam-Granada light scattering experimental results?

We considered quantitative comparisons with Amsterdam-Granada database. However, without knowing the internal structures of the particles used to generate the database, the comparisons would not be very valuable. It should be added that homogeneous Voronoi tessellation particles have been found to agree with Amsterdam-Granada database decently well, as shown in Ishimoto et al., "Shape modeling of mineral dust particles for light-scattering calculations using the spatial Poisson-Voronoi tessellation", JQSRT, 111, 2010, 24342443. We have now mentioned this correspondence in the text.

19. Section 6. Page 22. Line 29. is in..→is on the macroscopic scale.

Done

Comments on tables Tables 1-5. The total volume fraction of each of the *i*th elements contained in each of the tables do not sum to exactly 100%. Please

correct. This may have a slight impact on the EMA refractive index but will not alter any of the conclusions presented in the paper.

The values shown in the table are rounded from the values used in the calculations, which causes the apparent mismatch. No calculations were affected, including the EMA refractive indices. This has been clarified in the captions.

Comments on Figures.

Figure 1. The yellow labels in (b) are difficult to read suggest you use bold black and in (c).

We agree that the labels were difficult to read. The font size has been increased and changed to bold type. However, we kept the color yellow, because it was still the clearest of the colors we tested (including black).

Figure 4. Differences are difficult to see. Suggest you plot results as $\text{Log}_{10}(S_{11})$?

Figure 4 currently shows S_{11} on a log10-scale, which is equal to showing $\log_{10}(S_{11})$ on a linear scale. We have adjusted the y-axis limits to show the data better.

Figure 10. In climate models heating rates are important. A measure of this is the emission, which is related to the co-albedo, so rather than plotting ω_0 , suggest you plot $(1 - \omega_0)$ as that is the more useful parameter in atmospheric energetics?

At the recommendation of the referee, we have changed albedo in the figures and the text to co-albedo.

2 Referee #2, Dr. Maxim Yurkin

“The manuscript makes a step towards accurate simulation of atmospheric dust particles to be used for processing various remote sensing data. The main value (novelty) is in the well-described numerical experiment, which quantifies the effect of inhomogeneity. The latter is essential for making well-informed decision on accuracy of existent and future remote-sensing retrievals. While interpretation of these data leaves many questions (see below), the manuscript is worth publishing in Atmospheric Chemistry in Physics. However, several issues need to be addressed first:”

We thank the referee for this review and answer each of the points individually below

“1) The manuscript is based around numerical experiments, which requires the main set-up (the DDA method) to be described in sufficient details, including experimental errors. The latter is important, since large errors will

make all further quantitative comparisons meaningless. The authors do mention that the used discretization satisfy certain rule-of-thumb, however:

- any quantitative statements related to these rules were ever made only for a very limited set of test cases.

- they are surely meaningless for particles smaller than the wavelength. See (Yurkin & Hoekstra 2011) or in more details (Yurkin & Hoekstra, JQSRT 106:558-589, 2007).

Therefore, the authors should provide a quantitative estimate of the DDA accuracy over all test cases (and for all reported scattering quantities). At least, several representative cases should be studied using refined discretization, which can be conveniently done with jagged command line option of ADDA. More rigorous estimates can be obtained, e.g., with the extrapolation technique (Yurkin et al., J. Opt. Soc. Am. A 23:2592-2601, 2006)."

We have employed the jagged option of ADDA to study the inaccuracies related to shape determination. Unfortunately, even jagged 2 consumes roughly 8 times as much CPU time, which would be almost one million CPU hours for the full runs, which would take several months with the computing resources available to us. Instead, we have decided to perform limited tests, and only for jagged 2 (double dipole resolution along each axis, 8 times the total number of dipoles) instead of e.g. jagged 4 (quadruple dipole resolution along each axis, 64 times the total number of dipoles).

To get as detailed results as possible while preserving computer resources, we chose two individual size parameters to study, $x = 5$ and $x = 16$. The results for these, comparing each inhomogeneous run to the corresponding EMA runs, are shown in Figures 1 and 2 below for all of the scattering matrix elements. We see that for $x = 5$, the difference in resolution produces negligible changes in scattering, whereas the effect of using EMA is very large. In the case of $x = 16$, for some scattering matrix elements the finer resolution makes a noticeable difference, comparable to that of using EMA. However, if the EMA particle is also simulated with the double resolution, the EMA error remains relatively constant to the original resolution cases. Therefore, while the absolute values become more accurate, EMA does not perform better.

We conclude that the dipole resolution used caused relative errors of 1-10% at large size parameters, depending on the scattering matrix element in question, and <1% at small size parameters, where most of the particle sizes are located at in our particle size distribution. In contrast, the large particles have relatively small weights: size parameters 16 and larger have only a com-

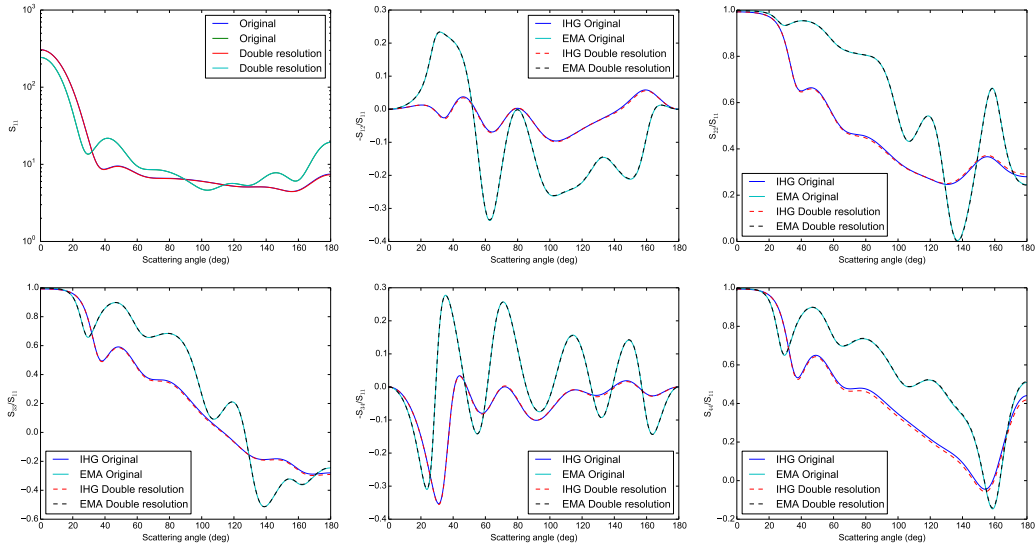


Figure 1: Results of the double resolution experiment for size parameter 5, showing all of the scattering matrix elements and using one of three Case 2 particles. The difference in doubling the dipole resolution is insignificant in comparison to the EMA error.

binned weight of 2.4% in the ensemble. Regardless, based on this, extra care should be taken with wider particle size distributions, and while the main features of simulations are unlikely to change, double dipole resolution should be considered at $x > 16$ to reduce uncertainties.

As a final note, of the scalar scattering quantities considered, only the linear depolarization ratio is changed noticeably by double dipole resolution (which increases by 13% at $x = 16$ due to S_{22} sensitivity); all others are virtually unaffected.

We have added brief discussion of these results to Section 3 of the manuscript: **Light scattering simulations.**

“2) Related to the above is the accuracy of shape representation (stochastic errors). The authors do consider three realizations of particular shape for each set of input parameters. However, their discussion is limited to . . . however, all of the results are qualitatively similar for each individual particle. (p.20362, line 24). The authors should add quantitative statements, so the reader may judge which part of differences between different particle models can be explained by random fluctuations.”

We agree with the criticism and provide clarification. In Figures 3 and 4 in this response we have shown Case 2 for two individual

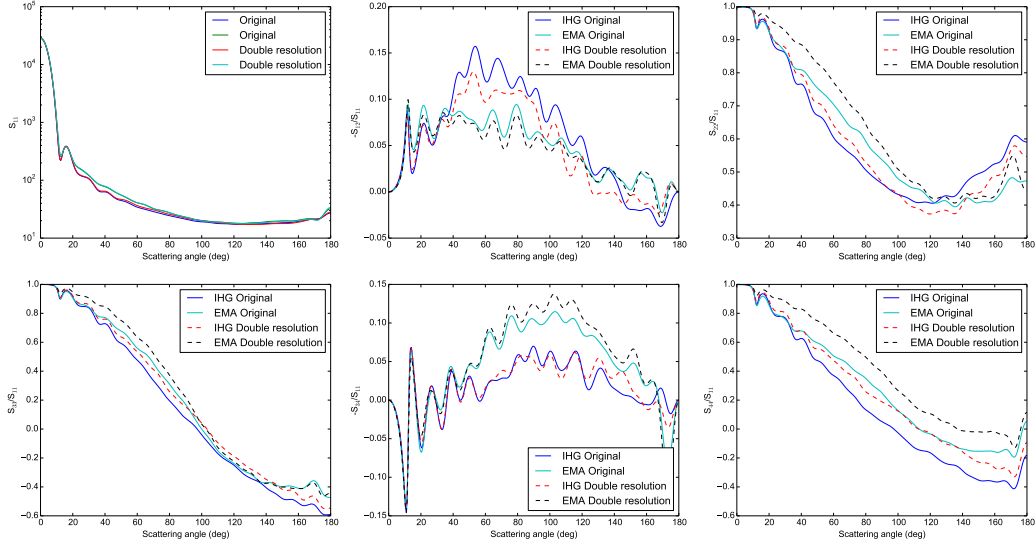


Figure 2: Results of the double resolution experiment for size parameter 16, showing all of the scattering matrix elements and using one of three Case 2 particles. The errors by using the original resolution instead of the doubled one can be up to 5-10% for some scattering matrix elements, which is comparable to the EMA error. However, when EMA particle is also simulated with double resolution, EMA error stays relatively constant. For other elements, the dipole resolution error is very small, similarly to the smaller size parameters.

size parameters (6 and 18) where the standard deviation of the three particles is used as the error bar (one SD above the line, one SD below the line, i.e. the total bar covers 68% of the variability). Naturally, SD is not a very good measure when $N=3$, but it should give a scale of the variability nevertheless. Individual sizes are shown instead of size-integrated values to see the difference at different sizes. It is noteworthy that the strong oscillation seen at some of these values is due to using single sizes and goes away at size integration, and thus is unrelated to the particle-to-particle variability.

Additionally, we have added some variability quantification to the text. We decided not to include the error bars to the (grayscale) figures in the article to keep them clear, and because the ensemble variability is not the focus of the article. The ensemble mainly provides oscillation reduction in scattering matrix elements, but since the inhomogeneous ensemble is compared against the homogenized

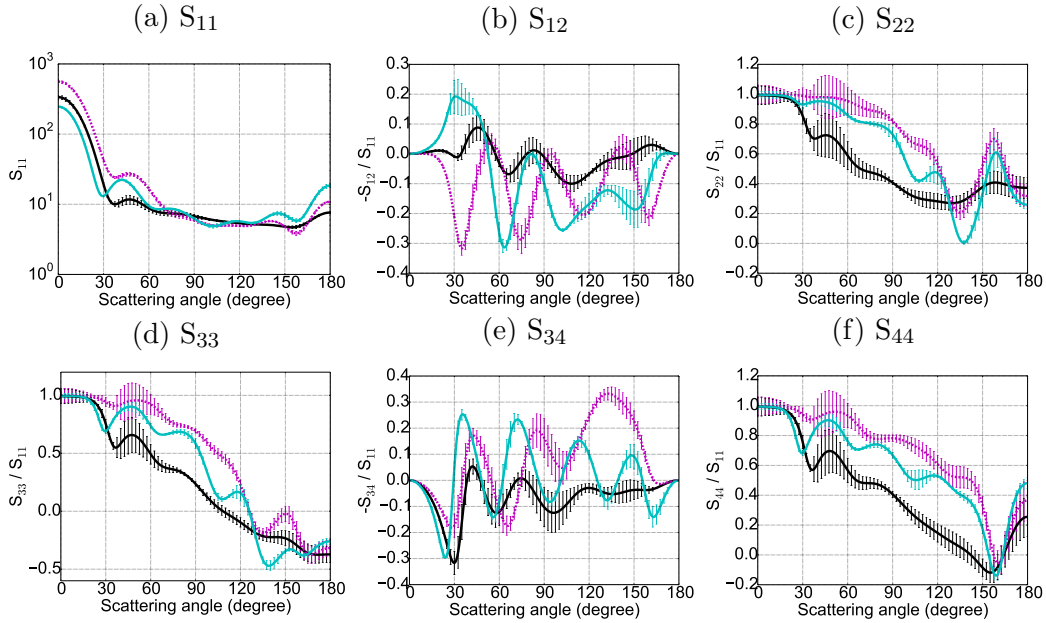


Figure 3: Scattering matrix elements for Case 2 ensemble at size parameter 5, with error bars added to denote ± 1 standard deviation variability of the individual particles in the ensemble. For most part, the variability is smaller than the differences between individual curves.

ensemble, the conclusions are unlikely to change even if we were to compare individual inhomogeneous particles to corresponding individual homogenized particles.

“3) The conclusion does summarize the presented results, but it is hard to employ those conclusions in practice. It does says that given approximate models are not sufficient, but says nothing about other alternatives. The relevant questions are:

- is it possible to fit effective refractive index to get better agreement?
- is it possible to fit a given inhomogeneous shape with a set of ellipsoids (and fitted refractive index)?
- is it possible to employ realistic shapes in practice (retrieval algorithms) or are certain simplifications required anyway?

The authors cant answer all these questions in this manuscript. But they should at least discuss them and show the directions of future research, which would lead to the answers. Otherwise, the manuscript only answers the question that is not very interesting.”

We agree that all of these questions pose interesting and potentially fruitful new venues of research, and some of them are

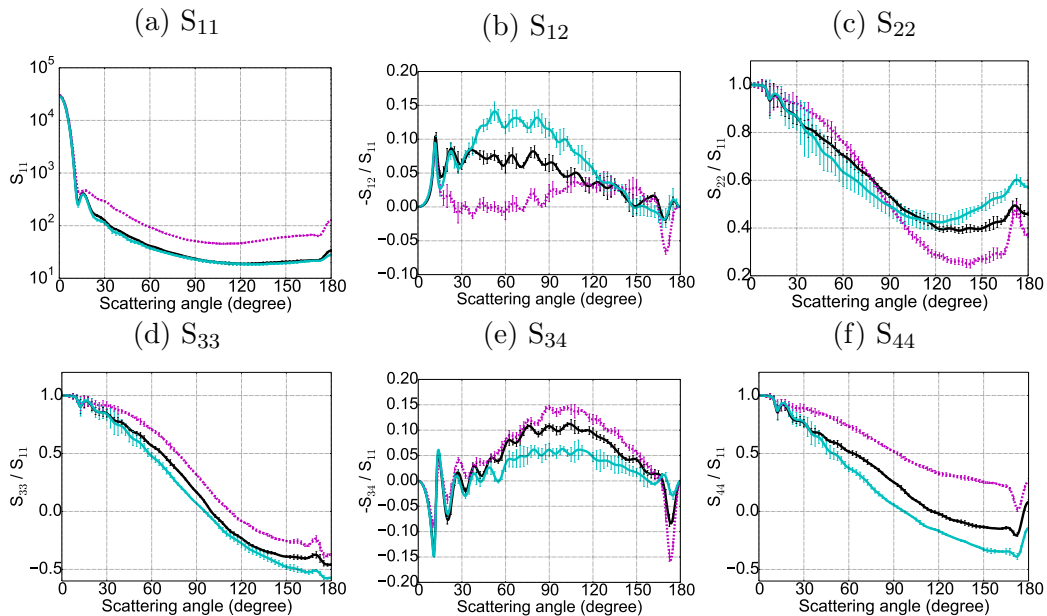


Figure 4: Scattering matrix elements for Case 2 ensemble at size parameter 16, with error bars added to denote ± 1 standard deviation variability of the individual particles in the ensemble. For most part, the variability is smaller than the differences between individual curves.

already being planned by the authors. The primary concern of the manuscript was to alert people to the fact that internal structures have a significant impact on scattering even by irregular scatterers (i.e. other than just by reducing regularity or modifying the effective refractive index), and we consider the question of how to answer these highlighted issues a separate one. We have added text to discussion that should clarify our interest in eventually answering the questions that the referee points out here.

“There are also several minor issues:

a) p.20363, line 23: smaller should probably be larger.

Fixed

b) p.20365, line 17: extend should be extent

Fixed

c) I recommend combining Tables 1-5 into one (list all minerals and have one column for each case). This will lead to more compact representation.”

We have combined the tables into one, as suggested.

3 Comment by Dr. Bastiaan van Diederhoven

“This is a short comment on the manuscript entitled Effects of dust particle internal structure on light scattering submitted to ACPD by Kemppinen et al. It is not my intent to provide a full review to the manuscript. The manuscript describes a sensitivity study to evaluate the optical impacts of some of the typical internal structures of atmospheric dust particles. Rigorous calculations of optical properties of internally-mixed, inhomogeneous dust particles are shown and compared to simple calculations for homogeneous versions of the particles by using an effective-medium approximation (EMA). A simple volume-average of the refractive indices is used here, given by Eq. 7. It is stated that this simple and straightforward mixing rule is chosen instead of any of the more sophisticated ones for simplicity: The more sophisticated EMAs are derived under different assumptions about the mixture, and therefore different EMAs might be optimal for different model particles considered here. It is true that different mixing rules are appropriate for different mixtures, but it has been shown that the volume mixing of refractive indices is very inappropriate for inhomogeneous mixtures of media with very different real and imaginary refractive indices (Chylek et al., 2000). Thus, the volume-mixing approach is clearly not suitable for the particles studied here, especially for the hematite mixtures. For these particles, the Bruggeman rule is most appropriate or alternatively the Maxwell-Garnett rule (e.g., Lesin et al., 2002). It makes no sense to use a mixing rule that is clearly not appropriate for the investigated cases.

This paper concludes that based on this work, it seems that it is exceedingly important that the effects of dust particle internal structures on light scattering are accounted for in a wide variety of applications. This conclusion is based on the comparison to the calculations using the inappropriate volume-mixing rule and therefore is not well supported. The authors should compare their rigorous calculations to those using the more appropriate mixing rules in order to investigate the importance of internal scattering processes in dust particles. Whether this simple adaptation would show that the Bruggeman and/or Maxwell-Garnett rules are capable of sufficiently reproducing the rigorous calculations or not, it will greatly enhance the impact of this work in my opinion. REFERENCE: Lesins et al., A study of internal and external mixing scenarios and its effect on aerosol optical properties and direct radiative forcing, JOURNAL OF GEOPHYSICAL RESEARCH, VOL. 107, NO. D10, 10.1029/2001JD000973, 2002”

We thank Dr. Diederhoven for his valuable comments on the

calculation of the effective medium approximation. The issue of EMA selection was also raised by the Referee #1, and we have decided to answer both simultaneously in a dedicated Section 4 in this response, below. We also agree that the conclusions require that the EMA selected is appropriate. The article by Lesins et al. has been added as a reference in Section 4.3 of the manuscript where we discuss the application and selection of the EMA calculation formula, and the Section itself has been extended to better substantiate the selection of the mixing rule.

4 Effective medium approximation comparisons

Both anonymous referee #1 and Dr. van Dienenhoven requested testing with different EMA's, such as Maxwell Garnett (MG) and Bruggeman formulas. We have performed these tests for a simplified version of our Cases 2 and 5, i.e. the particles with the hematite content, which are likely affected by the selection of EMA the most, as pointed out by Dr. van Dienenhoven.

Case 2 is simplified by considering only 2 materials instead of the original 12, because the traditional MG is applicable to only 2 materials. We have thus chosen as the materials to study a bulk clay mineral with refractive index of $1.55 + i0$ and volume fraction of 85%, and hematite with refractive index of $3.09 + i0.0925$ and volume fraction of 15%. The EMA of this simplified system obtained by volume average of refractive indices is $1.78 + i0.0139$, close to the original Case 2 EMA m of $1.78 + i0.0135$. Because the clay minerals in the original inhomogeneous particles have very similar refractive indices (most of the minerals are within between refractive indices 1.52 and 1.57, with roughly 6% of the total volume having refractive indices of up to 1.60), and based on the close match in the homogenized refractive indices between the original and the simplified versions, we conclude that it is likely that this simplified case is representative of the original case.

We have chosen to replicate the results with five different EMA's using this simplified composition: the original way of averaging refractive indices ($1.78 + i0.0139$), averaging permittivities ($1.86 + i0.0230$), MG using larger volume fraction as the matrix (MG1, $1.73 + i0.0073$), MG using larger volume fraction as the inclusion (MG2, $1.80 + i0.0172$), and Bruggeman ($1.74 + i0.0089$). It is very important to note that the particles in this study are generally not within the validity criteria of the EMA's, which also may help

to explain the results below. For example, the assumption that the inclusions are much smaller than the wavelength does not hold for the particles considered here. It could be argued that highly localized and spatially non-uniformly distributed inhomogeneity is very hard to represent by any simple parametrization, unless specifically tuned for each individual particle and even size parameter. These results are visualized in Figures 5 and 6 below for size parameters 5 and 16, respectively.

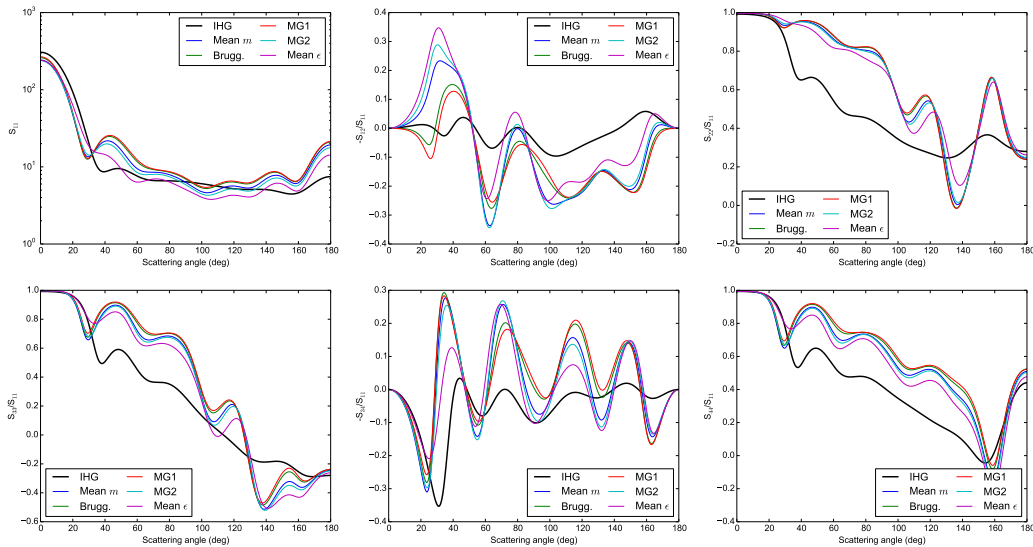


Figure 5: Case 2 scattering matrix elements with different effective medium approximations for size parameter 5

The results show that for $x = 5$, on average, all EMA's tested perform extremely badly. It seems that inhomogeneity dampens the oscillations by reducing regularity.

For $x = 16$, the results are more varied, depending on the scattering matrix element in question. We do not go into detailed analysis here, but the results can be summarized as follows. Overall, mean m and MG2 seem to be behaving the best, with MG1 and Bruggeman being the worst. Mean permittivity behaves optimally in some cases, such as small scattering angles of S_{44} , but badly in other cases. Furthermore, different EMA's give better matches at different scattering angles, which means that an EMA that works well at, say, backscattering direction, might not work well at all at other directions.

For comparison, we also tested another case, the one with thin hematite-rich coating (Case 5), again simplifying the particle to only two components to allow MG to be used. The components were clay with $m = 1.55 + i0.0$ and

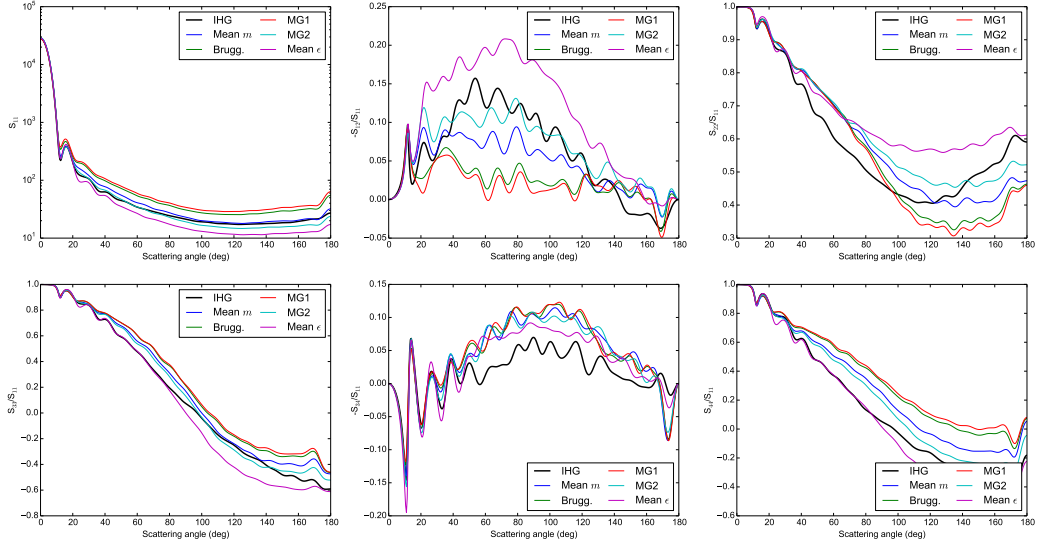


Figure 6: Case 2 scattering matrix elements with different effective medium approximations for size parameter 16

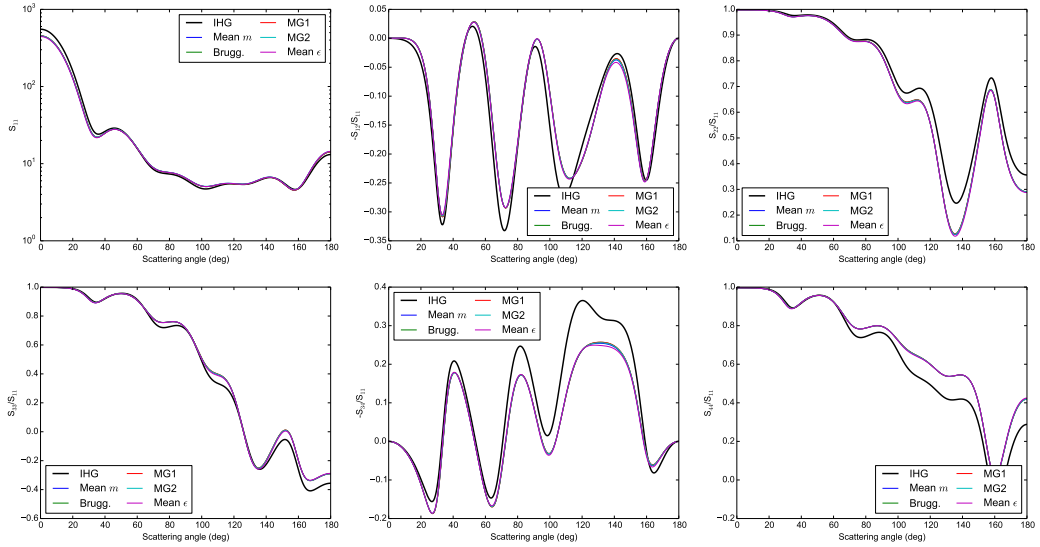


Figure 7: Case 5 scattering matrix elements with different effective medium approximations for size parameter 5

volume fraction 82%, and hematite-rich clay mixture with $m = 1.82 + i0.0139$ and volume fraction 18%. The different effective refractive indices were as follows: mean refractive index: $1.60 + i0.0025$, mean permittivity: $1.60 + i0.0028$, MG1: $1.60 + i0.0023$, MG2: $1.60 + i0.0025$, and finally Brugg-

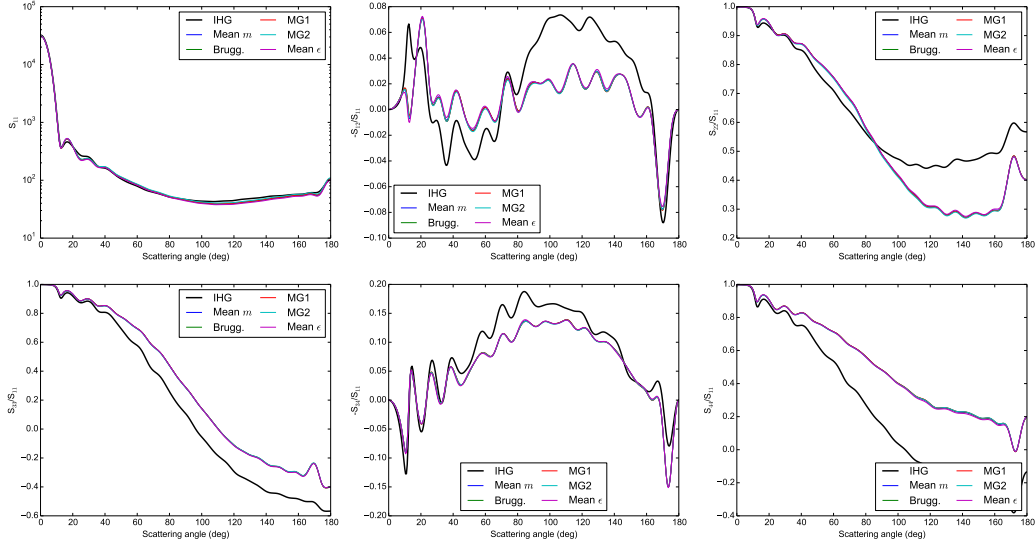


Figure 8: Case 5 scattering matrix elements with different effective medium approximations for size parameter 16

man: $1.60 + i0.0024$.

The results are shown in Figures 7 and 8. Interestingly, the results differ from those of Case 2. First, all of the EMA's tested behave very similarly to each other for both of the sizes tested, as expected given the very closely matching refractive indices. This is likely due to smaller refractive index contrast in the two materials, compared to Case 2. Further, EMA's seem to work better at small size parameters than large size parameters; behavior at small size parameters is very decent, but at large ones the errors are tens of percent. We speculate that this is likely due to thinness of the coating: at small size parameters the coating is too thin to interact strongly with radiation, which causes its effect to be modest and thus EMA's to work quite well. However, as the size increases and coating starts to have a larger effect, EMA's start producing wrong results.

Although only two cases and two individual sizes were tested, it seems safe to conclude that our findings related to the importance of explicit modeling of inhomogeneity does not depend on the choice of the EMA. Indeed, our choice was among the best for Case 2, i.e. the particle with hematite nodes, and likewise for Case 5 where all of the EMA's performed very similarly to each other. Finally, Lesin et al. notes that the volume averaging of refractive indices is the customary method in atmospheric applications. Therefore, using a familiar and wide-spread method is certainly substantiated, especially when no better alternative was found. Since no EMA tested here seems to

be behaving clearly better than the originally selected EMA, the conclusions of the article remain unaffected even if another EMA was selected. We have clarified and substantiated the EMA selection in the text, Section 4.3.

Manuscript prepared for Atmos. Chem. Phys. Discuss.
with version 2014/09/16 7.15 Copernicus papers of the L^AT_EX class copernicus.cls.
Date: 8 October 2015

Effects of dust particle internal structure on light scattering

O. Kemppinen^{1,2}, T. Nousiainen¹, and G. Y. Jeong³

¹Earth Observation, Finnish Meteorological Institute, P.O. Box 503, 00101, Helsinki, Finland

²Department of Applied Physics, Aalto University, Espoo, Finland

³Department of Earth and Environmental Sciences, Andong National University, Andong 760-749, Republic of Korea

Correspondence to: O. Kemppinen (osku.kemppinen@fmi.fi)

Abstract

There is a large variety of internal structures inside atmospheric dust particles, making them inherently inhomogeneous. Such structures may have a large effect on ground-level and atmospheric radiation. So far, dust particle internal structures and their effect on the light scattering properties have proved to be hard to quantify, in part due to challenges in obtaining information about these structures. Recently, internal structures of individual dust particles were revealed through focused ion beam milling and analyzed. Here, we perform a sensitivity study to evaluate the optical impacts of some of the typical internal structures revealed. To obtain suitable model particles, the first step is to generate inhomogeneous particles with varying internal structures by using an algorithm that is based on three-dimensional Voronoi tessellation. The parameters for the particle generation are obtained from studies of real-world Asian dust particles. The second step is to generate homogeneous versions of the generated particles by using an effective-medium approximation, for comparison. Third, light scattering by both versions of these particles is simulated with discrete-dipole approximation code. This allows us to see how different internal structures affect light scattering, and how important it is to account for these structures explicitly. Further, this allows us to estimate the potential inaccuracies caused by using only homogeneous model particles for atmospheric studies and remote sensing measurements. The results show that the effects vary greatly between different kinds of internal structures and single-scattering quantity considered, but for most structure types the effects are overall notable. Most significantly, hematite inclusions in particles impact light scattering heavily. Furthermore, internal pores and hematite-rich coating both affect some form of light scattering noticeably. Based on this work, it seems that it is exceedingly important that the effects of dust particle internal structures on light scattering are accounted for in a wide variety of applications.

1 Introduction

Mineral dust particles are an important part of the atmosphere (Zender et al., 2003). Their impact on incoming ground-level solar radiation, including aerosol radiative forcing, can be considerable (Durant et al., 2009; ?)(Durant et al., 2009; Haywood et al., 2011a, b; Osborne et al., 2011). At areas with high dust concentrations, their effect on the amount of incoming radiative energy at the surface can be roughly ten percent when the Sun is at the zenith, and even more when it is close to the horizon. Interestingly, this effect can either increase or decrease the amount of radiative energy reaching the surface (Forster et al., 2007). Due to its abundance and impact, accounting for dust is imperative in most radiative balance calculations and atmospheric remote sensing. However, due to the large variance in dust effects on radiation, the impacts are challenging to account for, particularly when using simplified models.

The reasons for the large variance of the impact of dust on radiation can be many, but in addition to the obvious variations in particle size and concentration, shapes, [surface roughness characteristics](#) and internal structures may play a role. It is known that many dust particles contain materials with significant dielectric contrast, for example iron oxides or internal pores. Transmission electron microscopic (TEM) analysis of cross-sections of single particles showed that internal pores of varying sizes are common features of Asian dust particles. Additionally, submicron iron oxides, such as hematite and goethite, are often distributed within clay medium (Jeong and Nousiainen, 2014). Furthermore, it has been shown by, e.g., Vilaplana et al. (2006); Nousiainen et al. (2011a, b, 2003); Muinonen et al. (2009) that inhomogeneity can affect light scattering by particles significantly, and that scattering by such particles is not easily mimicked by ensembles of simple homogeneous model particles.

While particle size distributions and many other population-level parameters are possible to measure by remote sensing (Chou et al., 2008; Kim et al., 2008), shapes and internal structures are much harder to determine. For example, derivation of the true three-dimensional shape requires application of atomic force microscopy (e.g. Chou et al., 2008;

Woodward et al., 2015), or stereogrammetry from electron microscope images (Lindqvist et al., 2014). Internal structures can be analyzed, e.g., by slicing open dust particles with a focused ion beam, as done by Jeong and Nousiainen (2014). The impacts of real shapes and internal structures on scattering have barely been touched, because it is very hard to retrieve the three-dimensional composition, and especially to measure light scattering by the same particles whose structures are retrieved. Without coinciding coincident data, the connection between optical properties and physical properties cannot be established.

Here we carry out a sensitivity study on the impacts of internal structures. Our approach is to create an algorithm that allows us to generate discrete-dipole approximation (DDA) models of particles with desired types and amounts of internal structures, for which accurate light scattering simulations can be then easily run, thus allowing taking internal structures into account explicitly and accurately. What we aim to do is to generate a set of particles that are complex-shaped and irregular, as are real dust particles, and possess internal structure characteristics that resemble those observed in real dust. The clear benefit of this pure modeling approach is that it allows us to calculate accurate values for individual optical properties, linked to known individual physical properties. We will be testing how various internal structures change light scattering compared to a baseline version, which is composed only of optically similar minerals. Further, knowing the composition of the inhomogeneous particles perfectly completely allows us to calculate homogeneous versions of the same particles with an effective-medium approximation (EMA), and simulate light scattering by both the inhomogeneous and the homogeneous versions of the particles. This, then, allows us to quantify the errors in light scattering caused by using the homogeneous version of the particle instead of the true form of the particle.

The main purpose of this study is to investigate the effects of different types of internal structures on the single-scattering properties. We will be examining particles with various internal structures, such as empty cavities and materials with high real and imaginary refractive index, such as hematite and other iron oxides. The article is structured as follows: Sect. 2 introduces the physical dust particles on which the computational particle generator is based on, Sect. 3 summarizes the relevant single-scattering theory, Sect. 4 explains the

model particle generator algorithm in detail, Sect. 5 shows the results of the scattering calculations for inhomogeneous and homogeneous particles and, finally, Sect. 6 contains the summary of the work, and discussion of the significance of the results.

2 Internal structures in Asian dust particles

Asian dust is an important mineral dust lifted from arid regions in the northwestern China and southern Mongolia, and transported in a long range across East Asia and the North Pacific (Jeong et al., 2014, and references therein). The details of the particle interiors were recently discovered by Jeong and Nousiainen (2014). Most of the dust particles are composites of several mineral types of varying grain sizes. Relatively coarser minerals are quartz, plagioclase, K-feldspar, calcite, and muscovite, while finer minerals are illite-smectite series clay minerals and iron oxides. The basic internal structures of dust particles result from the agglomeration of these mineral grains in the source soils. Within the dust particles, coarser minerals tend to form separated grains, while very fine grains of clay minerals and iron oxides form tight aggregates. In clay-rich dust particles, coarser grains such as quartz, plagioclase and muscovite are enclosed in the clay medium, while in clay-poor particles, quartz and plagioclase grains are commonly crusted with coatings of clay agglomerates. Submicron irregular pores are common in the dust particles. Example internal structure and mineral distribution of an Asian dust particle (3.8 μm in diameter, Fig. 1a) is presented in Fig. 1b, showing a porous agglomerate of several mineral types. **These particles were collected directly from air on a borosilicate glass-fiber filter using a total suspended particulate (TSP) sampler (Jeong and Nousiainen, 2014).**

Jeong and Nousiainen (2014) grouped internal structures into single and polycrystalline cores of quartz, feldspars, calcite, and amphibole often with oriented clay coatings; clay agglomerates showing **preferred to random orientations commonly with coarser mineral inclusions partially preferred orientations**; and platy coarse phyllosilicates. Iron oxides in Asian dust are mostly goethite and hematite. Although their contents are low in mineral dust, their potential **impact** to optical properties is known to be significant (Sokolik and Toon, 1999; Lafon et al.,

2006). Although they occur as their own agglomerates, they are commonly distributed as submicron grains through the clay medium as shown in Fig. 1c–d. Certainly, there must be wide ranges of internal structures and mineral compositions from porous to nonporous, coated to non-coated, preferred to randomly oriented, from monocrystalline to polycrystalline, and iron-poor to iron-rich (Jeong and Nousiainen, 2014). Currently, the statistics of structural types are not available yet because the number of dust particles subjected to TEM analysis is not sufficient. Evidently, further extensive TEM works in combination with high resolution scanning electron microscopy (SEM) are required to **establish the population of the discover and characterize the various** internal structures.

3 Single-scattering concepts

The foundation of all radiative effects comes from single-scattering interactions. The scattering matrix for a particle,

$$\begin{pmatrix} I_s \\ Q_s \\ U_s \\ V_s \end{pmatrix} = \frac{1}{k^2 d^2} \begin{bmatrix} S_{11} & S_{12} & S_{13} & S_{14} \\ S_{21} & S_{22} & S_{23} & S_{24} \\ S_{31} & S_{32} & S_{33} & S_{34} \\ S_{41} & S_{42} & S_{43} & S_{44} \end{bmatrix} \begin{pmatrix} I_i \\ Q_i \\ U_i \\ V_i \end{pmatrix}, \quad (1)$$

characterizes the single-scattering event by linking the properties of incident (i) and scattered (s) radiation by the particle. Here $[I, Q, U, V]^T$ is the Stokes vector describing the properties of light: I describes the intensity, Q and U the linear polarization, and V the circular polarization of the wave. The wavenumber $k = 2\pi\lambda^{-1}$ is related to the radiation wavelength λ , and d is the distance from the scattering particle. Although the full matrix contains 16 elements, they are not independent, and under certain conditions, the matrix simplifies to only 6 independent elements: S_{11} , S_{12} , S_{22} , S_{33} , S_{34} , and S_{44} (Hovenier and van der Mee, 2000). These conditions are that the particles be randomly oriented, and that either the particles are mirror symmetric, or the particles and their mirror particles are present **with in** equal numbers. However, it has been shown by, e.g., Muñoz et al. (2012);

Nousiainen and Kandler (2015) that even when these conditions are not strictly true, for ensembles of complex particles, such as dust, the scattering matrix closely conforms to the simplified form.

Here, we study the effects of internal structures primarily in terms of individual scattering matrix elements, from [where which](#) all other effects can be determined. We also link these effects to relevant radiative transfer and remote sensing quantities by calculating four scalar scattering quantities, which are described below.

The single-scattering albedo, $\bar{\omega}$, describes the amount of energy being scattered in a single scattering event compared to that being absorbed. To be precise, it is the ratio of scattering and extinction cross-sections:

$$\bar{\omega} = \frac{C_{\text{sca}}}{C_{\text{ext}}}, \quad (2)$$

where C_{sca} is the scattering cross-section, a measure of the total power scattered by the particle, and C_{ext} is the sum of scattering and absorption cross-sections. [In this work we use a derivative quantity, called the co-albedo, which is defined as \$1 - \bar{\omega}\$.](#)

The asymmetry parameter g is used to describe how the scattered intensity varies between the forward ($\theta < 90^\circ$) and backward ($\theta > 90^\circ$) hemispheres of the scatterer, where θ is the scattering angle, [i.e.](#), the angular difference in propagation directions between the incident and the scattered radiation. The asymmetry parameter is obtained from S_{11} by:

$$g = \frac{2\pi}{k^2 C_{\text{sca}}} \int_0^\pi \sin \theta \cos \theta S_{11}(\theta) d\theta. \quad (3)$$

In many lidar applications, a quantity called lidar ratio, R , is used. The lidar ratio is the ratio of the extinction to the backscattering cross-section:

$$R = \frac{C_{\text{ext}}}{C_{\text{back}}} = \frac{k^2 C_{\text{ext}}}{S_{11}(180^\circ)}, \quad (4)$$

where $S_{11}(180^\circ)$ is the value of S_{11} at $\theta = 180^\circ$, that is, the intensity at the exact backscattering direction.

Linear depolarization ratio, δ_L , is another quantity typically used in lidar applications. One reason is that the scattering matrix element S_{22} is usually very sensitive to the shape of the particle, and therefore the linear depolarization ratio can be used to extract information about the particle shape, or at least to detect the presence of non-spherical particles. Linear depolarization ratio is defined as

$$\delta_L = \frac{S_{11}(180^\circ) - S_{22}(180^\circ)}{S_{11}(180^\circ) + S_{22}(180^\circ)}. \quad (5)$$

As an example, [single](#) spherical, isotropic particles have $S_{11} = S_{22}$, which means that the linear depolarization ratio would be exactly zero.

Light scattering simulations

We performed the light scattering simulations of the generated inhomogeneous and homogeneous particles with a discrete-dipole approximation (DDA) (Purcell and Pennypacker, 1973) light scattering software ADDA 1.2 MPI (Yurkin and Hoekstra, 2011). DDA is a flexible method for simulating light scattering by irregularly shaped particles, discretized into a regular lattice of individual dipoles. DDA is also capable of handling arbitrary collections of different materials: In an extreme case every lattice element can have a different refractive index. Therefore, DDA is extremely well suited for a detailed study of internal structures, such as performed in this paper.

DDA is generally accurate as long as the target dipole resolution is sufficient. In this work, the target shapes for all size parameters were composed of roughly two hundred and twenty thousand dipoles. The value $y = |m|kl$, where m is the refractive index, k is the wavenumber and l is the dipole size, is typically used to evaluate the applicability of the DDA method. The largest y value for the particles in this study was approximately 0.7, which is below the commonly cited DDA accuracy limit of $y \leq 1$ (Zubko et al., 2010).

Test simulations with higher dipole resolution for our inhomogeneous targets showed that $y = 0.7$ already yields relative errors of several percent in differential scattering quantities. The use of higher dipole resolution at size parameters roughly $x \geq 16$ would therefore be beneficial, albeit very costly in terms of CPU time consumption. Regarding the size-distribution averaged results, on the other hand, where these largest sizes have only marginal weight, the relative errors are only about one percent. Our choice of dipole resolution is thus deemed quite sufficient.

We used a three-particle ensemble for results, and each internal structure case of each of these three particles was simulated with size parameters $\{0.5, 1, 2, 3, \dots, 20\}$. Furthermore, scattering by each inhomogeneous and homogeneous particle was averaged over 8192 random orientations for each size parameters.

The simulations were run on the Finnish Meteorological Institute Cray XC30 supercomputer Voima. In the calculations we used 64 computer cores per simulation, and 10 concurrent simulations were run in parallel. With this setup, the total amount of CPU time used was approximately 110 000 h for three distinct versions of the five cases and their EMA versions.

4 Particle generation model and scattering simulations

4.1 Generating the particle geometry

Our method for generating the particle models involves multiple stages that can be run separately if needed. The overview of each main stage is given below. The algorithm assumes that the particle can be represented by a regular three-dimensional lattice of individual volume elements, or dipoles. With a good enough dipole resolution, the representation can replicate most large-scale structures of real dust particles with a sufficient accuracy. This representation also allows us to trivially convert the algorithm output to a DDA format for light scattering simulations. The generation process is summarized in Fig. 2.

Stage 1: tessellation

To generate computational models of realistic particles with internal structure, we employ an algorithm with three-dimensional Voronoi tessellation at its core (Aurenhammer, 1991). The underlying idea is that the tessellation cells are roughly analog to the mineral grains within real (agglomerate) particles. While this is only an approximation, with the right mean size and shape of the grain, the method can be plausible. Voronoi tessellation has been used for irregular dust particle shape generation by e.g. Ishimoto et al. (2010), but our novel approach is to use the tessellation for generating internal particle structures instead of just the overall shape.

The generation of model shapes begins with an enclosed, discretized space composed of empty volume elements. The first step of the algorithm is to randomly place a given number of points within this volume. These act as *seeds* for the next step, which is to go through every *element* in the volume and to find the seed closest to it, as measured by a weighted distance, described below. The set of elements for which a given seed is closest forms a *cell* of that seed. Each element within a cell has the same composition as the seed, but different seeds can have different compositions.

The formula for weighted distance is:

$$d_w = \sqrt{w_x \Delta x^2 + w_y \Delta y^2 + w_z \Delta z^2}, \quad (6)$$

where $\Delta \cdot$ correspond to the distances along different axes, and $w \cdot$ correspond to the weight specific to different axes. In this formalism, a lower weight for an axis causes the grains to be elongated along that axis. The above equation is easily generalizable to have axis directions corresponding to arbitrary vectors, but in this case we have limited the directions to the major axes of the dipole lattice, hence the simplified form above. In this work we used $w_x = w_y = 1$, $w_z = 2/3$, to produce slightly elongated cells.

After the whole volume has been divided into cells, the volume is culled to extract a model particle from it. Here we have used an ellipsoid with the same axis proportions as the ellipsoidal grain axis proportions as the culling shape. The generated particles have aspect

ratios close to 1.5. The culling is done in such a way that each cell with at least one element outside of the culling shape is removed from the volume, and the remaining cells form the particle. In this work we used 800 seeds within the original volume, yielding mean cell size of roughly 1200 elements, which translates to roughly 0.5 % of the final culled particle volume.

Stage 2: cell separation

The next step is to separate the cells from each other. This is accomplished by finding the geometrical center of the particle, and forming unit vectors that point from it to the seeds of each cell. The cells are then moved to the direction specified by their corresponding vectors by a user-specified distance, and the final locations are discretized by rounding the cell element to the nearest integer. Therefore, the cells do not change sizes or shapes, but are separated from each other. This step is to allow separating individual cells or crystals from each other, which is often the case also with real dust particles and thus yields more realistic model shapes. The displacement length used in this work was 5, where 1 is the size of one lattice element, or a dipole in the DDA targets.

Stage 3: concave hull

The cell separation creates gaps between the cells, and the next step is to fill these gaps, and to soften sharp edges and other roughness characteristics around the particle. This is accomplished with a method called concave hull (Lindqvist et al., 2009). The concave hull method works by testing each element of the original volume in the following way: if a sphere with a constant radius r , a so-called generating sphere, centered at the element, does not overlap with any non-empty element, each element within the sphere is flagged. Otherwise, nothing is done. After all the elements have been checked with the generating sphere, all previously empty elements that have not been flagged are assigned to consist of a filling material with user-specified composition. The r used in this work was 3 element lengths, which was enough to fill the inner seams caused by cell separation, and to partially fill some deep “valleys” at the surface.

Stage 4: coating

The fifth step is to coat the particles. The method for coating is simple: a layer of coating is added by setting each empty element that is orthogonally adjacent to a non-empty element as non-empty, assigning these elements to be composed of a coating material. Multi-layer coatings are formed by using the method iteratively. We used a three-layer coating in this work for both the normal coating and the hematite-rich coating cases.

Stage 5: nodes (optional)

There is an additional optional step, which can be used to add further internal structures in the form of inclusions. To generate inclusions in the original shape we insert nodes inside the particle. Nodes are generated simply by finding a random element in the particle, and growing a sphere of a given radius around the element, replacing parts of any existing cell with the node cell.

Here we have used nodes to generate both hematite inclusions and internal pores. The approach allows us to add these features into generated model particles without introducing any other changes in their shapes. For both the hematite nodes and internal pores, we generated 20 nodes with a radius of 8 element lengths, which made the nodes comparable in size to cells.

4.2 Assigning the mineral composition

The above section contains the technical description of the shape-generating algorithm. The model is given physical relevance by introducing *materials*. Henceforth, each cell is stochastically assigned a material in such a way that the model particles would represent real dust particles composition as specified by the input parameters of the model. Mineral volume composition representative of Asian dust was derived from TEM and SEM data in Jeong and Achterberg (2014). Additionally, the concave hull filling cell, the coating cell, and the node cells from above are given a material corresponding to real-world materials.

The end product of this process is a list of volume elements that contain their position and refractive index. This is exactly what is needed for DDA simulations, hence making it straightforward to simulate scattering by these particles.

4.3 Homogenization

Once the particles with internal structure have been generated with the algorithm described above, we will generate their homogenized versions. This is achieved with a simple effective-medium approximation (EMA). We calculate the effective refractive index m_{eff} of the homogenized particle as a volume-weighted average of the refractive indices of the constituent elements: (Chýlek et al., 2000)

$$m_{\text{eff}} = \sum_i f_i m_i, \quad (7)$$

where f_i is the volume fraction of the i th material, and m_i is the refractive index of the i th material.

This simple and straightforward mixing rule is chosen instead of any of the more sophisticated ones for simplicity: The more sophisticated EMA's are derived under different assumptions about the mixture, and therefore different Different mixing rules are known to perform differently depending on the particle type (Lesins et al., 2002). To ascertain that our results are not critically dependent on the choice of the mixing rule, we compared the performance of five different mixing rules for two different particles having the same shapes as our particles but being composed of only two constituent minerals: a clay particle with 15% of hematite as inclusions; and another clay particle with thin hematite-rich coating, where the hematite-containing material volume fraction was 18%. The mixing rules tested were the Maxwell Garnett, inverse Maxwell Garnett, Bruggeman, volume-weighted average refractive index (Eq. (7)) and volume-weighted average permittivity. Scattering simulations were conducted with effective refractive indices produced by these rules, and compared with simulations where the inhomogeneity is explicitly accounted for. Differences in the obtained scattering matrix elements were then used to quantify the performance of the EMA in question.

For the first test particle, there was a very large variability between different EMA's, with the average refractive index and the inverse Maxwell Garnett EMA's might be optimal for different model particles considered here performing the best. For the second test particle, all of the mixing rules performed decently at small sizes, but poorly at large sizes, and very similarly to each other at all sizes. Therefore, our conclusions is that out of the five mixing rules tested, not one performed better than the one selected here, and therefore the one selected here is appropriate for more detailed comparisons.

5 Results

5.1 Particle generation results and the model correspondence with real dust particles

In total, we studied five distinct internal structure cases. The five cases are:

- *Case 1*: an inhomogeneous particle composed of dielectrically similar minerals (no strong contrasts in the refractive index)
- *Case 2*: Case 1 particle with 15 % hematite added as spherical inclusions (replacing the original material)
- *Case 3*: Case 1 particle with 17 % air added as spherical internal pores (replacing the original material)
- *Case 4*: Case 1 particle with both hematite (15 %) and pores (17 %) added
- *Case 5*: Case 1 particle with the original coating material replaced by a hematite-rich material

For each case, the particle resembles the “baseline” Case 1 in other respects than the added features. Therefore, for instance, apart from the added hematite, the mineral volume fractions in Case 2 resemble those in Case 1. While they are not identical due to the

stochastic nature of inclusion locations, they are close enough to plausibly assume that the changes seen are not caused by the differing non-hematite mineral content but instead are caused by hematite. In fact, in the text below we compare the other cases to Case 1 for specifically this reason.

For all of these cases, we use a three-particle ensemble for all of the results. We decided to use an ensemble to average out oscillations by single particles, and to see if the effects of different internal structures are consistent across all three different generated particles. Therefore, the particle generator is run three times with the same input parameters, the DDA simulations are run for the all three versions of the five cases, and for each case we calculate the average of the three results. Because the generator is stochastic in nature, the three individual particles differ from each other despite having identical input parameters; however, all of the results are qualitatively similar for each individual particle **in such a way that inter-particle variability is smaller than the difference between inhomogeneous and homogenized cases, or between inhomogeneous case and the baseline, for all scattering matrix elements and at most scattering angles.**

Tables ??-?? show Table 1 shows the ensemble-averaged mineral composition of the five different internal structure cases we have used here, as well as the EMA refractive indices for each case. The refractive indices for the minerals at $\lambda = 550$ nm are retrieved from MinDat database (<http://www.mindat.org>, accessed 21 May 2015). Empty is used to denote internal pores, CM to denote clay mixture, and HRCM to denote hematite-rich clay mixture. CM refractive index is calculated with EMA from the mineral composition of the first stage (tessellation) of the Case 1 particle, and HRCM refractive index is calculated likewise from the first stage of the Case 1 particle, but with 15 % hematite content added. CM is used as the filling material, and as the coating material of all cases apart from Case 5. HRCM is used as the coating material of Case 4.

Due to the very large variability of the types and structures of real-world dust particles and the lack of information of the three-dimensional structures of the particles, quantitative validation of the generated shapes is challenging. Instead, we can compare the particle compositions to those of real particles, and compare the cross-sections visually. Looking at

Fig. 3a, which depicts one example cross-section of Case 1 particle, we see that the grains are oriented and shaped in a somewhat random way. Figure 3b shows the same particle, but with a three-dimensional rendering with a part of the particle cut off to show some of the internal structure. The grains of different materials seem to be scattered relatively randomly through the particle. Additionally, the characteristic sizes of the grains are generally 0.5–1 μm with the largest r used in this study, 1.75 μm . Comparing these parameters to the electron microscopy images by Jeong and Nousiainen (2014), especially the rock fragment dust particle (Fig. 13 in the reference), we see clear similarities. Although the model particle grains are slightly less irregular than some grains in the real particles, we see that the overall shapes, sizes and orientations are similar. However, the model particle grains are proportionally **smaller larger** than those in the real rock fragment dust particle, with radii of roughly 1/6 of the particle radius instead of roughly 1/14 of the particle radius that the rock fragment dust particle has. Still, since the model particles themselves are smaller than the particles shown in Jeong and Nousiainen (2014), the absolute sizes of the grains end up being close to each other. One thing to note is that the coating thickness of the real dust particles seems to be roughly 0.5 μm , instead of roughly 0.1 μm of the model particles. Regardless, as we show below, even this very thin coating causes clear effects when it contains hematite, and the effects would likely be only larger if the coating layer were thicker. Overall, although there are differences in details, we believe that our model particles are useful and sufficiently similar to observed real characteristics to serve as proxies in the sensitivity studies conducted here. Additionally, it could be argued that the correspondence of the particles does not matter significantly as long as they are not extremely unrealistic, such as very thin rods or **perfect** spheres, as long as the internal features are of the correct size scale.

In addition to the grains and the coating, the model particles contain inclusions and pores, as described above. The nodes are generated to be comparable to grains in size, that is, diameters of 0.5–1 μm at the largest size parameters studied (not shown). While internal pore sizes and shapes vary greatly in real dust particles, at least the iron-oxide-rich dust

particle (Fig. 12 in Jeong and Nousiainen, 2014) shows pores with characteristic lengths of roughly $1 \mu\text{m}$.

5.2 Results of the light-scattering simulations

Here we show the effect of taking inhomogeneity into account in light scattering simulations for several different internal structure scenarios. The scattering matrix elements will be analyzed as a function of the scattering angle after integrating the values over a size distribution. As the size distribution we use a lognormal distribution with the geometric mean radius $r_g = 0.4$ and the geometric standard deviation $\sigma_g = 2$, resulting in $r_{\text{eff}} = 0.82 \mu\text{m}$. This distribution follows the one by Lindqvist et al. (2014); Kempainen et al. (2015b), and is designed to provide reasonable contributions both from small and large size parameters, while also providing an effective radius reasonably close to those in real-world applications. Therefore, we kept the wavelength constant at $\lambda = 550 \text{ nm}$, while varying the particle r .

As the simulations are carried out separately for each particle size and only then averaged over the size distribution, we can easily estimate how a different choice of size distribution would impact the results. For example, had a wider size distribution been chosen, the results would have changed to some degree due to assigning a larger weight to larger particles compared to the current size distribution. Exact changes would depend on the inhomogeneity case and scattering matrix element in question, but based on the results for individual sizes, for example Case 5 EMA errors would have been increased. We speculate this is due to larger interaction between the radiation and the thin hematite-rich coating, causing the EMA to perform worse for large size parameters than for small size parameters.

It should be reiterated that the primary purpose here is not to study the single-scattering properties themselves, but how they differ when the internal structure is accounted for either explicitly or through an effective medium approximation. In particular, we are interested in establishing which types of internal structures have large effects on scattering. For each of the five cases, we show light scattering by the inhomogeneous particle (called IHG), light scattering by IHG Case 1 (called the baseline), as well as the homogeneous version of the

particle (called EMA), for straightforward comparison of the effects of inhomogeneity. As a reminder, the baseline and the EMA versions of the particles are identical in size and shape to the corresponding IHG versions, and the only difference is in the local refractive indices within the lattice elements.

Below, we study each of the six independent scattering matrix elements separately. For each matrix element, we show all of the five cases, comparing the IHG version of the particle with the baseline and the EMA versions. Case 1, the baseline, is not discussed separately along the other cases because EMA values for it are virtually identical to the IHG values for all of the scattering matrix elements. S_{11} is shown as it is, using a logarithmic scale, and the other elements are shown as ratios $S./S_{11}$, where $S.$ is the element in question. Additionally, the ratios with S_{12} and S_{34} are shown as negatives, instead, as per the usual convention.

Added contrast shows a clear effect on S_{11} , as seen in Fig. 4. In particular, added hematite nodes (Cases 2 and 4) and, to a lesser **extend extent** internal pores (Case 3), seem to decrease S_{11} compared to the baseline Case 1. The values at side-scattering and back-scattering angles are especially reduced. In addition to this reduction, the form of the scattering function is **smoothened smoothed** in these cases. It is notable that the smoother form of the scattering function resembles that of the real dust particles better than the Case 1 version (Muñoz et al., 2012), **and tessellation particle simulations have been shown to overall compare reasonably well to laboratory scattering measurements (Ishimoto et al., 2010)**. Case 5, with the hematite-rich coating, does not differ noticeably from the baseline. For particles that differ from the baseline, Cases 2, 3 and 4, the performance of EMA for replicating the baseline varies. For the particle with added pores (Case 3), EMA seems to work reasonably well in replicating the IHG values, with only slight differences being seen at the side-scattering angles. However, for Cases 2 and 4, which include hematite inclusions, EMA values are clearly different from the true IHG values, in particular at the backscattering direction, where the EMA values can be up to 30 % too large.

For $-S_{12}/S_{11}$ (Fig. 5), internal pores (Cases 3 and 4) seem to have the largest effects on scattering compared to the baseline, with the particle with only the hematite nodes (Case

2) also showing clear impact. For all of these cases, added internal structure increases $-S_{12}/S_{11}$ at most scattering angles. The particle with the hematite coating, Case 5, shows smaller difference to the baseline than the cases mentioned above, and the effect is of the opposite direction: the hematite-rich coating decreases $-S_{12}/S_{11}$ instead of increasing it. EMA seems to replicate the true scattering function of the IHG version relatively poorly for all of the Cases 2–5. For Cases 2–4, $-S_{12}/S_{11}$ for the EMA particle are lower than those of the corresponding IHG particles. However, for Case 5, EMA seems to smoothen out the angular dependency, and therefore the direction of the error varies depending on the scattering angle.

Figure 6 shows that hematite has a very significant effect on S_{22}/S_{11} regardless of it being present as inclusions (Cases 2 and 4) or as a part of the coating material (Case 5). For Cases 2 and 4, the angle dependence of the scattering matrix values is overall smoother than that of the baseline case. Case 3, with only the internal pores, also shows similar behavior to Cases 2 and 4, but with a much smaller magnitude. The particle with hematite coating (Case 5) also shows clear difference, but instead of the angular dependency being changed, the values are overall higher than the baseline. For S_{22}/S_{11} , the EMA versions of the particles generally do not replicate the true IHG values well. For Cases 2 and 4, the EMA values are slightly closer to the true values than the baseline, but the difference is still significant. For Case 3, EMA seems to, in fact, be further from the true values than the baseline. Finally, for Case 5, the EMA values are virtually identical to the baseline values.

S_{33}/S_{11} values (Fig. 7) for the IHG versions of the particles are generally lower than the baseline. The particle with internal pores, Case 3, is an exception, and for it the baseline and IHG are virtually identical. Interestingly, the difference between EMA values and the baseline is very small for all of the cases, in particular Cases 4 and 5, for which it is indistinguishable. For all of the cases, EMA results in larger than true values.

It is clear from Fig. 8 that the impact of internal structure on $-S_{34}/S_{11}$ varies significantly depending on the exact type of the structure. Hematite nodes in Cases 2 and 4 smoothen out the angular dependency greatly apart from forward-scattering angles, where the values are amplified. Because of this smoothening, the $-S_{34}/S_{11}$ values are overall smaller for

the Case 2 and 4 IHG particles than those of the baseline. For the particle with internal pores, Case 3, the values are also smaller than the baseline, but the angular profile is not smoothed. For the hematite-coated Case 5, the IHG values are higher than those of the baseline, unlike for all of the other cases. Like with Case 3, the Case 5 angular dependency is not smoothed. Compared to the IHG and baseline values, the validity of EMA varies from case to case. For Cases 2 and 4, EMA works decently well, and although the values are not particularly close to those of IHG, at least they are closer than those of the baseline. However, for Cases 3 and 5, EMA values are more erroneous than even the baseline.

Lastly, the effects of the added forms of internal structure on S_{44}/S_{11} are shown in Fig. 9, and are quite consistent for all of the cases studied. All of the IHG values are lower than those of the baseline, although for Case 3 the difference is clearly smaller than for the other cases. Again, the EMA versions of the particles do not replicate the S_{44}/S_{11} values of the IHG versions closely. For Cases 2 and 3 the EMA values are slightly higher than the real values, while for Cases 4 and 5 the difference is higher. Interestingly, for Case 3 again, the scattering matrix element values for the EMA particle are further from the real values than the baseline.

As a practical consideration of identifying particle internal structures from measurements, we recommend polarization measurements. While producing an identification algorithm would require a very large amount of additional work, it seems that, for example, positive degree of linear polarization ($-S_{12}/S_{11}$) values at scattering angles between 60 and 120 degrees correlate with refractive index contrasts inside the particles, whether that is from hematite nodes or internal cavities. However, it needs to be stressed that these observations apply only for single-scattering measurements; inferring particle internal structures from multiple-scattering polarization measurements will be much less straightforward.

5.3 Scalar scattering quantities

In addition to the effect of internal structures on the scattering matrix elements, we also explore the impacts of the same types of internal structures on four scalar quantities that are often used in climate or remote sensing applications. These quantities, namely [albedoCO-](#)

albedo, asymmetry parameter, linear depolarization ratio and lidar ratio, are shown below as a function of the particle size parameter. The format is similar to that used for the scattering matrix elements, where we show results separately for the IHG, the baseline, and the EMA particles, and compare them to see how added internal structures affect the values. In addition to the size-parameter-dependent figures, we also show the values of the size-distribution-averaged results in Table 2 for each case. In addition to the values themselves, the table also shows the difference, and the relative difference, that is, the difference as a percentage to the IHG value.

Single-scattering **albedos** **co-albedo** for the original (IHG), Case 1 (baseline), and homogenized (EMA) versions of the three-particle ensembles of the five internal structure cases are shown in Fig. 10. Neither Case 1 nor Case 3 contain any absorbing materials, and therefore their **albedoes are uniformly one****co-albedo are uniformly zero**, and do not require any further discussion. Case 2 and Case 4 behave similarly to each other. For them, the **albedo decreases** **co-albedo increases** as the particle size increases due to the hematite inclusions approaching the wavelength size. For sizes where the inclusions are larger than the wavelength of the incoming radiation, roughly size parameter 10 and larger, the **albedo** **co-albedo** stabilizes to an almost constant value. For these cases, EMA **overestimates albedo** **underestimates co-albedo** of the IHG version by **5–10****15–50** % between size parameters roughly 5 and 15. At small sizes, the inclusions are much smaller than the wavelength, and therefore the EMA and the IHG values are close to each other. At the largest sizes, it seems like EMA **co-albedo** is approaching the values of the IHG particle and becoming even **smaller****larger**. It would be interesting to see if at very large size parameters this development continues and EMA ends up **underestimating albedo****overestimating co-albedo significantly**. For Case 5, the **albedo decreases** **co-albedo increases** almost linearly as the size parameter increases, when the coating starts to interact with light more strongly. With increased coating thickness or even larger particle sizes, it is reasonable to assume that the **albedo would decrease** **co-albedo would increase** even further. Case 5 also shows a small, but consistent, difference in **albedo** **co-albedo** between the IHG and the EMA particles, with EMA being **lower****higher**.

Asymmetry parameter for the original and homogenized versions of the five internal structure cases are shown in Fig. 11. For the particles with hematite nodes, Cases 2 and 4, the asymmetry parameter is higher than that of the baseline by roughly 20 % at most size parameters. For the particles with only the pores added (Case 3) and the particles with the hematite coating (Case 5), the asymmetry parameter is virtually identical to the baseline. For all of the particles shown here, EMA performs reasonably well for the asymmetry parameters, following the IHG values closely.

The linear depolarization ratio for the original and homogenized versions of the five internal structure cases are shown in Fig. 12. Added hematite seems to have a very significant increase on linear depolarization ratio, regardless of whether it is present as inclusions (Cases 2 and 4) or as part of the coating material (Case 5). The effect of hematite is to decrease linear depolarization ratio by up to 40 % at large size parameters, and coating seems to have a stronger impact than inclusions. Internal pores have a smaller effect, and increase the linear depolarization rate by roughly 10 %. For Cases 2 and 4, EMA is closer to the true IHG values than the baseline, but the difference is still notable. However, for Cases 3 and 5, EMA performs badly and has values very close to those of the baseline.

Lidar ratio for the original and homogenized versions of the five internal structure cases are shown in Fig. 13. Hematite nodes (Cases 2 and 4) seem to affect the lidar ratio greatly, whereas internal pores or hematite coating (Cases 3 and 5) do not. At large size parameters, the presence of hematite nodes roughly triples the lidar ratio from the baseline values, and even at smaller size parameters, the difference is notable. For Cases 2 and 4, EMA results are typically between those for the baseline and IHG, meaning that the EMA manages to partially account for the impact of the additional internal structure. Still, EMA results differ from those of IHG by 20–50 %. The direction of the difference between IHG and EMA depend on the exact size parameter. For Cases 3 and 5, EMA values are indistinguishable from the IHG values.

6 Summary and conclusions

In this work, we studied the effects of dust particle internal structure in a computational way based on real internal structures revealed by Jeong and Nousiainen (2014). First, we generated qualitatively realistic dust particles with various internal structures by using a sophisticated computational model. Second, homogeneous versions of these particles were generated with an effective-medium approximation. Third, light scattering simulations for both versions of the particles were run with a discrete-dipole approximation program called ADDA.

Five distinct internal structure cases were studied, and for each case we used a three-particle ensemble. First, we studied particle whose composite minerals had similar refractive indices. This was considered our baseline, to which the other cases were compared to. Second, we added hematite inclusions to the baseline particles. Third, we added internal pores to the baseline. Fourth, both hematite inclusions and internal pores were added to the baseline. Fifth, the coating material of the baseline was replaced with a hematite-containing material, but no nodes or pores were added.

These models of internal structures were selected by their common occurrence in the Asian dust particles on the basis of systematic TEM data provided in Jeong and Nousiainen (2014) Although many more cases are possible, we restricted the analysis to five cases to include major features of internal structures while keeping the computation load manageable. Natural dust particles contain two major mineral types of iron oxides: goethite and hematite. We selected hematite as a representative iron oxide in the structural model because its high refractive indices and effect on optical properties were treated previously (Sokolik and Toon, 1999; Lafon et al., 2006). Of course, iron oxide contents of dust particles vary in a wide range, thus 15 volume % hematite observed in natural particle is likely a case of rather high content of iron oxides. However, the purpose of the calculation here was to show clearly the effect of hematite on diverse optical properties.

For each of these cases, we studied light scattering by both the inhomogeneous and homogenized versions of the particles and compared them against the baseline. The results

show that most types of internal structure have clear effects on light scattering, and that many of those effects are not properly accounted for by the effective-medium approximation (EMA) that we used. Our findings are consistent with those of Kocifaj and Videen (2008) that the performance of EMA is inconsistent when the inhomogeneity is in on macroscopic scale. Possible errors from the use of EMA's for such particles are thus hard to predict, and will depend on the quantity of interest. Overall, hematite inclusions turned out to be the most impactful of the forms of internal structure studied here, affecting all of the scattering matrix elements and scalar scattering quantities. Hematite-rich coating affects all of the scattering matrix elements apart from S_{11} , and for linear depolarization ratio has an even greater effect than hematite inclusions. Internal pores affect especially $-S_{12}/S_{11}$ very significantly, but also the other scattering matrix elements to a lesser degree; scalar scattering quantities considered, on the other hand, remain relatively close to the baseline. Additionally, in many cases, having both hematite nodes and internal pores present amplifies the effects compared to having only the hematite nodes, instead of dampening the effects in some way. Finally, having a particle composed of several different materials, but with similar refractive indices, is the exception. In our analysis such a particle could safely be treated as homogeneous, and even using a very simple mixing rule for the effective refractive index calculations provided accurate results.

All four of the scalar variables studied, the single-scattering albedo, asymmetry parameter, linear depolarization ratio and lidar ratio, were affected noticeably by some forms of internal structure. For albedo, adding hematite content lowered the values significantly. For asymmetry parameter, hematite nodes, but not hematite-rich coating, increased the values clearly. For linear depolarization ratio, all forms of hematite lowered the values greatly. Finally, for lidar ratio, added hematite nodes increased the values two- or three-fold. Interestingly, we can compare the differences to those caused by adding surface roughness, as done by Kemppinen et al. (2015a). Overall, internal structures, especially hematite nodes, seem to have a greater effect on scattering matrix elements than modest surface roughness. However, the impact of surface roughness on scattering at the backscattering direction can be very notable, comparable to internal hematite. For example,

increasing surface roughness has a similarly sized effect on linear depolarization ratio as that of adding hematite, but of the opposite direction.

Based on these results, it appears that the internal structure of real dust particles need to be accounted for in single-scattering simulations to obtain accurate results. Not only is it common in real dust particles, it also has major effects on scattering matrix elements and many scalar scattering quantities. Furthermore, the form of the internal structure matters. For example, light scattering changes considerably depending on whether hematite is present as inclusions, or mixed in the coating material. Additionally, at least for the simple mixing rule tested here, a homogenized particle created with an effective-medium approximation is unable to well mimic scattering by the original inhomogeneous version of the particle in most cases. In fact, in some cases using an effective-medium approximation causes results to be more wrong than ignoring the internal structure altogether. Therefore, if accuracy is desired in the results, accounting for internal structure should be done explicitly.

Following up on these results, there are several directions to consider. As a practical concern, one might try to find an EMA that works very well for some or all of the inhomogeneity types here. Additionally, replicating the scattering by the inhomogeneous particles by using detailed modeling results to fine-tune shape and composition ensembles of simple model shapes, such as ellipsoids, might lead to much better results in applications. However, as shown by Kemppinen et al. (2015b), such a fitting procedure is risky, and needs to be done with caution. Without either of the above options, the results are still hard to apply in practical applications, such as retrieval algorithms or climate models. On the positive side, the differences seen between inhomogeneity types may help in identifying dust particle types from remote measurements, especially polarization and lidar measurements. While this requires a great deal of work, there is clearly hope that such a method could be developed.

Acknowledgements. The authors wish to thank Maxim Yurkin, Bastiaan van Diedenhoven and an anonymous referee for their helpful comments in improving the manuscript. This research has been funded by the Academy of Finland (grant 255718), the Finnish Funding Agency for Technology

and Innovation (Tekes; grant 3155/31/2009), the Magnus Ehrnrooth Foundation, and the National Research Foundation of Korea grant NRF-2011-0028597. Maxim Yurkin is acknowledged for making his ADDA code publicly available (<https://code.google.com/p/a-dda/>).

References

- Aurenhammer, F.: Voronoi diagrams a survey of a fundamental geometric data structure, *ACM Comput. Surv.*, 23, 345–405, 1991.
- Chou, C., Formenti, P., Maille, M., Ausset, P., Helas, G., Harrison, M., and Osborne, S.: Size distribution, shape, and composition of mineral dust aerosols collected during the African monsoon multidisciplinary analysis special observation period 0: dust and biomass-burning experiment field campaign in Niger, January 2006, *J. Geophys. Res.-Atmos.*, 113, D00C10, doi:10.1029/2008JD009897, 2008.
- Chýlek, P., Videen, G., Geldart, D. J. W., Dobbie, J. S., and Tso, H. C. W.: Effective medium approximations for heterogeneous particles, in: *Light Scattering by Nonspherical Particles*, edited by: Mishchenko, M. I., Hovenier, J. W., and Travis, L. D., chap. 9, Academic Press, San Diego, USA, 273–308, 2000.
- Durant, A., Harrison, S., Watson, I., and Balkanski, Y.: Sensitivity of direct radiative forcing by mineral dust to particle characteristics, *Prog. Phys. Geog.*, 33, 80–102, 2009.
- Forster, P., Ramaswamy, V., Artaxo, P., Berntsen, T., Betts, R., Fahey, D., Haywood, J., Lean, J., Lowe, D., Myhre, G., Nganga, J., Prinn, R., Raga, G., Schulz, M., and Dorland, R. V.: Changes in atmospheric constituents and in radiative forcing, in: *Climate Change 2007: The Physical Science Basis. Contribution of Working Group I to the Fourth Assessment Report of the Intergovernmental Panel on Climate Change*, edited by: Solomon, S., Qin, D., Manning, M., Chen, Z., Marquis, M., Averyt, K., Tignor, M., and Miller, H., chap. 2, Cambridge University Press, Cambridge, UK and New York, NY, USA, 130–234, 2007.
- Haywood, J., Johnson, B., Osborne, S., Baran, A., Brooks, M., Milton, S., Mulcahy, J., Walters, D., Allan, R. P., Klaver, A., et al.: Motivation, rationale and key results from the GERBILS Saharan dust measurement campaign, *Quarterly Journal of the Royal Meteorological Society*, 137, 1106–1116, 2011a.

- Haywood, J. M., Johnson, B. T., Osborne, S. R., Mulcahy, J., Brooks, M. E., Harrison, M. A. J., Milton, S. F., and Brindley, H. E.: Observations and modelling of the solar and terrestrial radiative effects of Saharan dust: a radiative closure case-study over oceans during the GERBILS campaign, *Q. J. Roy. Meteor. Soc.*, 137, 1211–1226, doi:10.1002/qj.770, 2011. 2011b.
- Hovenier, J. and van der Mee, C.: Basic relationships for matrices describing scattering by small particles, in: *Light Scattering by Nonspherical Particles*, edited by: Mishchenko, M. I., Hovenier, J. W., and Travis, L. D., chap. 3, Academic Press, San Diego, USA, 61–85, 2000.
- Ishimoto, H., Zaizen, Y., Uchiyama, A., Masuda, K., and Mano, Y.: Shape modeling of mineral dust particles for light-scattering calculations using the spatial Poisson–Voronoi tessellation, *J. Quant. Spectrosc. Ra.*, 111, 2434–2443, 2010.
- Jeong, G. Y. and Achterberg, E. P.: Chemistry and mineralogy of clay minerals in Asian and Saharan dusts and the implications for iron supply to the oceans, *Atmos. Chem. Phys.*, 14, 12415–12428, doi:10.5194/acp-14-12415-2014, 2014.
- Jeong, G. Y. and Nousiainen, T.: TEM analysis of the internal structures and mineralogy of Asian dust particles and the implications for optical modeling, *Atmos. Chem. Phys.*, 14, 7233–7254, doi:10.5194/acp-14-7233-2014, 2014.
- Jeong, G. Y., Kim, J. Y., Seo, J., Kim, G. M., Jin, H. C., and Chun, Y.: Long-range transport of giant particles in Asian dust identified by physical, mineralogical, and meteorological analysis, *Atmos. Chem. Phys.*, 14, 505–521, doi:10.5194/acp-14-505-2014, 2014.
- Kemppinen, O., Nousiainen, T., and Lindqvist, H.: The impact of surface roughness on scattering by realistically shaped wavelength-scale dust particles, *J. Quant. Spectrosc. Ra.*, 150C, 55–67, doi:10.1016/j.jqsrt.2014.05.024, 2015a.
- Kemppinen, O., Nousiainen, T., Merikallio, S., and [Risnen Räsänen, P.](#): [On retrieving refractive index Retrieving microphysical properties of dust-like particles using shape distributions of ellipsoids ellipsoids: the case of refractive index](#), *Atmos. Chem. Phys. Discuss.*, 15, 16861–16900, , 2015b 11 117–11 132, doi:doi:10.5194/acp-15-11117-2015, 2015b.
- Kim, S.-W., Yoon, S.-C., and Kim, J.: Columnar Asian dust particle properties observed by sun/sky radiometers from 2000 to 2006 in Korea, *Atmos. Environ.*, 42, 492–504, 2008.
- Kocifaj, M. and Videen, G.: Optical behavior of composite carbonaceous aerosols: DDA and EMT approaches, *J. Quant. Spectrosc. Ra.*, 109, 1404–1416, doi:10.1016/j.jqsrt.2007.11.007, 2008.
- Lafon, S., Sokolik, I. N., Rajot, J. L., Caquineau, S., and Gaudichet, A.: Characterization of iron oxides in mineral dust aerosols: implications for light absorption, *J. Geophys. Res.-Atmos.*, 111, D21207, doi:10.1029/2005JD007016, 2006.

- Lesins, G., Chylek, P., and Lohmann, U.: A study of internal and external mixing scenarios and its effect on aerosol optical properties and direct radiative forcing, *Journal of Geophysical Research: Atmospheres* (1984–2012), 107, AAC–5, 2002.
- Lindqvist, H., Muinonen, K., and Nousiainen, T.: Light scattering by coated Gaussian and aggregate particles, *J. Quant. Spectrosc. Ra.*, 110, 1398–1410, doi:10.1016/j.jqsrt.2009.01.015, 2009.
- Lindqvist, H., Jokinen, O., Kandler, K., Scheuvs, D., and Nousiainen, T.: Single scattering by realistic, inhomogeneous mineral dust particles with stereogrammetric shapes, *Atmos. Chem. Phys.*, 14, 143–157, doi:10.5194/acp-14-143-2014, 2014.
- Muinonen, K., Nousiainen, T., Lindqvist, H., Muñoz, O., and Videen, G.: Light scattering by Gaussian particles with internal inclusions and roughened surfaces using ray optics, *J. Quant. Spectrosc. Ra.*, 110, 1628–1639, doi:10.1016/j.jqsrt.2009.03.012, 2009.
- Muñoz, O., Moreno, F., Guirado, D., Dabrowska, D., Volten, H., and Hovenier, J.: The Amsterdam–Granada light scattering database, *J. Quant. Spectrosc. Ra.*, 113, 565–574, 2012.
- Nousiainen, T. and Kandler, K.: Light scattering by atmospheric mineral dust particles, in: *Light Scattering Reviews 9*, edited by: Kokhanovsky, A. A., Springer Praxis Books, Springer, Berlin, Heidelberg, Germany, 3–52, doi:10.1007/978-3-642-37985-7, 2015.
- Nousiainen, T., Muinonen, K., and Räisänen, P.: Scattering of light by large Saharan dust particles in a modified ray optics approximation, *J. Geophys. Res.*, 108, 4025, doi:10.1029/2001JD001277, 2003.
- Nousiainen, T., Kahnert, M., and Lindqvist, H.: Can particle shape information be retrieved from light-scattering observations using spheroidal model particles?, *J. Quant. Spectrosc. Ra.*, 112, 2213–2225, doi:10.1016/j.jqsrt.2011.05.008, 2011a.
- Nousiainen, T., Muñoz, O., Lindqvist, H., Mauno, P., and Videen, G.: Light scattering by large Saharan dust particles: comparison of modeling and experimental data for two samples, *J. Quant. Spectrosc. Ra.*, 112, 420–433, doi:10.1016/j.jqsrt.2010.09.003, 2011b.
- Osborne, S., Baran, A., Johnson, B., Haywood, J., Hesse, E., and Newman, S.: Short-wave and long-wave radiative properties of Saharan dust aerosol, *Quarterly Journal of the Royal Meteorological Society*, 137, 1149–1167, 2011.
- Purcell, E. M. and Pennypacker, C. R.: Scattering and absorption of light by nonspherical dielectric grains, *Astrophys. J.*, 186, 705–714, 1973.
- Sokolik, I. R. and Toon, O. B.: Incorporation of mineralogical composition into models of the radiative properties of mineral aerosol from UV to IR wavelengths, *J. Geophys. Res.*, 104, 9423–9444, 1999.

- Vilaplana, R., Moreno, F., and Molina, A.: Study of the sensitivity of size-averaged scattering matrix elements of nonspherical particles to changes in shape, porosity and refractive index, *J. Quant. Spectrosc. Ra.*, 100, 415–428, doi:10.1016/j.jqsrt.2005.11.068, 2006.
- Woodward, X., Kostinski, A., China, S., Mazzoleni, C., and Cantrell, W.: Characterization of dust particles' 3D shape and roughness with nanometer resolution, *Aerosol Sci. Tech.*, 49, 229–238, 2015.
- Yurkin, M. A. and Hoekstra, A. G.: The discrete-dipole-approximation code ADDA: capabilities and known limitations, *J. Quant. Spectrosc. Ra.*, 112, 2234–2247, 2011.
- Zender, C. S., Bian, H., and Newman, D.: The mineral Dust Entrainment And Deposition (DEAD) model: description and 1990s dust climatology, *J. Geophys. Res.*, 108, 4416, doi:10.1029/2002JD002775, 2003.
- Zubko, E., Petrov, D., Grynko, Y., Shkuratov, Y., Okamoto, H., Muinonen, K., Nousiainen, T., Kimura, H., Yamamoto, T., and Videen, G.: Validity criteria of the discrete dipole approximation, *Appl. Optics*, 49, 1267–1279, 2010.

Table 1. The mineral content contents for each of the particle inhomogeneous cases. CM refers to clay mixture, Empty refers to internal pores, and HRCM refers to hematite-rich clay mixture. Volume fraction (VF) columns 1-5 correspond to Cases 1-5. Percentages may not sum to 100% due to rounding in Case 1. Despite the large number displayed values. EMA m values in the bottom part of different minerals, all of the table show the homogenized refractive indices are close to of each other case.

Mineral	Refractive index	VF1 (%)	VF2 (%)	VF3 (%)	VF4 (%)	VF 5 (%)
CM	1.55	31.19	39.05	36.42	21.78	13.26
Illite	1.57	21.06	14.88	14.88	14.88	21.06
Quartz	1.55	13.31	9.00	9.00	9.00	13.31
Smectite	1.52	12.77	7.96	7.96	7.96	12.77
Plagioclase	1.53	8.93	6.17	6.17	6.17	8.93
Calcite	1.60	3.85	2.37	2.37	2.37	3.85
Gypsum	1.52	2.78	1.66	1.66	1.66	2.78
Chlorite	1.58	2.19	1.59	1.59	1.59	2.19
K-eldspar	1.52	1.89	1.34	1.34	1.34	1.89
Kaolinite	1.56	1.86	1.16	1.16	1.16	1.86
Amphibole	1.62	0.18	0.16	0.16	0.16	0.18
Hematite	$3.09 + i0.0925$	0.00	14.65	0.00	14.65	0.00
Empty	1.00	0.00	0.00	17.27	17.27	0.00
HRCM	$1.82 + i0.0139$	0.00	0.00	0.00	0.00	17.93

	Case 1	Case 2	Case 3	Case 4	Case 5
EMA m	1.55	$1.78 + i0.0135$	1.46	$1.68 + i0.0135$	$1.60 + i0.0025$

Table 2. Scalar scattering quantities for the size distribution averaged three-particle ensembles. Inhomogeneous (IHG), Case 1 (baseline) and homogeneous (EMA) values are shown separately, as well as their differences as percentages of the IHG value.

Case	IHG	Baseline	EMA	(IHG – Baseline) / IHG (%)	(IHG – EMA) / IHG (%)
Co-albedo					
Case 1	1.00 0.00	1.00 1.00 0.00	0.00	N/A	N/A
Case 2	0.82 0.18	1.00 0.00	0.86 0.14	–22.21	100.00
Case 3	1.00 0.00	1.00 1.00 0.00	0.00	N/A	N/A
Case 4	0.82 0.18	1.00 0.00	0.87 0.13	–21.96	100.00
Case 5	0.98 0.02	1.00 0.00	0.97 0.03	–2.43	100.00
Asymmetry parameter					
Case 1	0.62	0.62	0.62	0.00	0.04
Case 2	0.57	0.62	0.58	–8.46	–0.66
Case 3	0.64	0.62	0.68	–2.89	–5.88
Case 4	0.59	0.62	0.61	–6.19	–4.09
Case 5	0.62	0.62	0.61	–0.25	2.41
Linear depolarization ratio					
Case 1	0.31	0.31	0.31	0.00	0.19
Case 2	0.35	0.31	0.35	13.30	–0.04
Case 3	0.25	0.31	0.25	–24.33	–0.58
Case 4	0.32	0.31	0.35	3.54	–10.60
Case 5	0.26	0.31	0.33	–19.88	–29.21
Lidar ratio					
Case 1	45.51	45.51	45.59	0.00	–0.17
Case 2	44.26	45.51	34.08	–2.83	23.00
Case 3	57.09	45.51	66.28	20.28	–16.10
Case 4	47.81	45.51	39.89	4.80	16.57
Case 5	40.58	45.51	39.83	–12.14	1.85

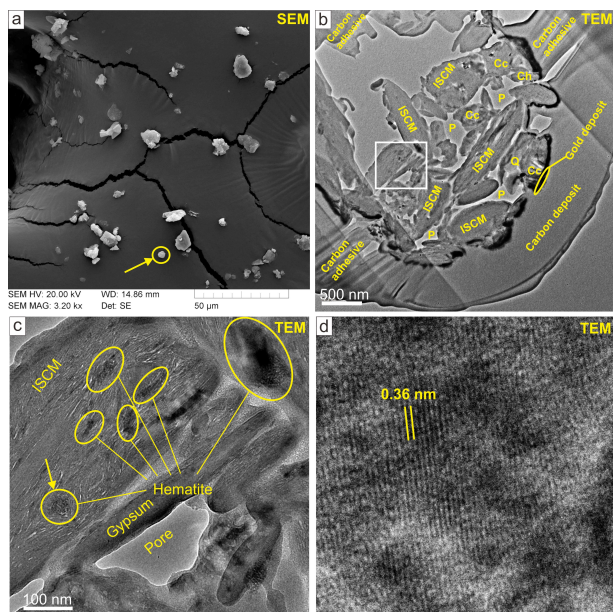


Figure 1. Example internal structure and mineral distribution in Asian dust particle. Panel (a) is an SEM image showing a dust particle of 3.8 μm in diameter (arrow) processed with focused ion beam to prepare a thin slice for TEM analysis. Panel (b) is a TEM image of the slice showing mineral grains and interstitial pores. Cc = calcite, Ch = chlorite, ISCM = illite-smectite series clay minerals, P = pore, Q = quartz. Gold deposition was applied for electrical conduction for SEM observation. Carbon was deposited before focused ion beam process. Panel (c) is a magnified image from the square in Panel (b) showing the submicron hematite grains enclosed in the illite-smectite series clay minerals. Panel (d) is a lattice fringe image of hematite indicated as arrow in Panel (c).

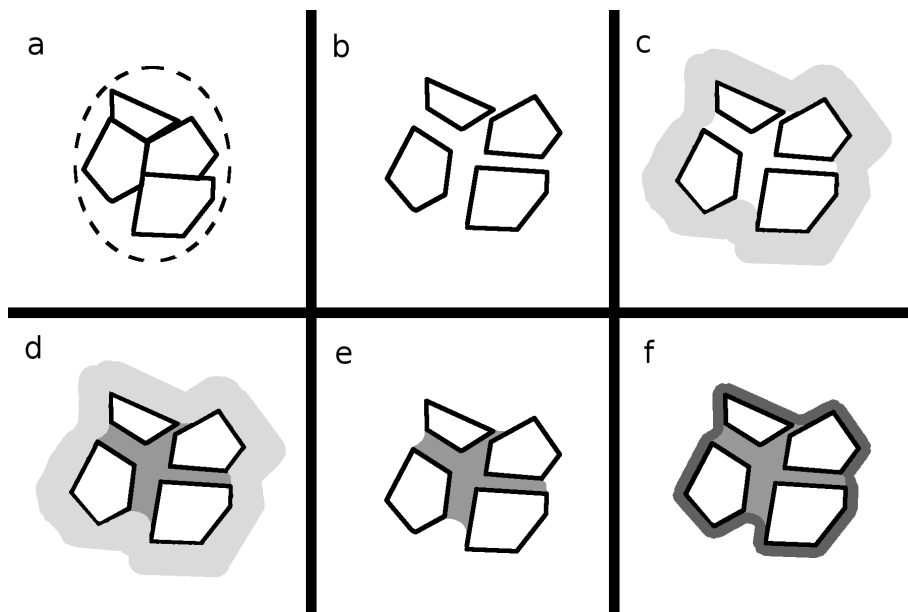


Figure 2. A schematic two-dimensional figure of the particle generation process. Panel (a) shows a simple four-cell tessellation, with the dashed ellipse showing an example culling surface. Panel (b) shows the cell separation. Panel (c) shows the formation of the concave hull, while Panel (d) shows the filling process based on the hull. Panel (e), shows the particle with no coating, and finally, Panel (f) shows the particle with coating added.

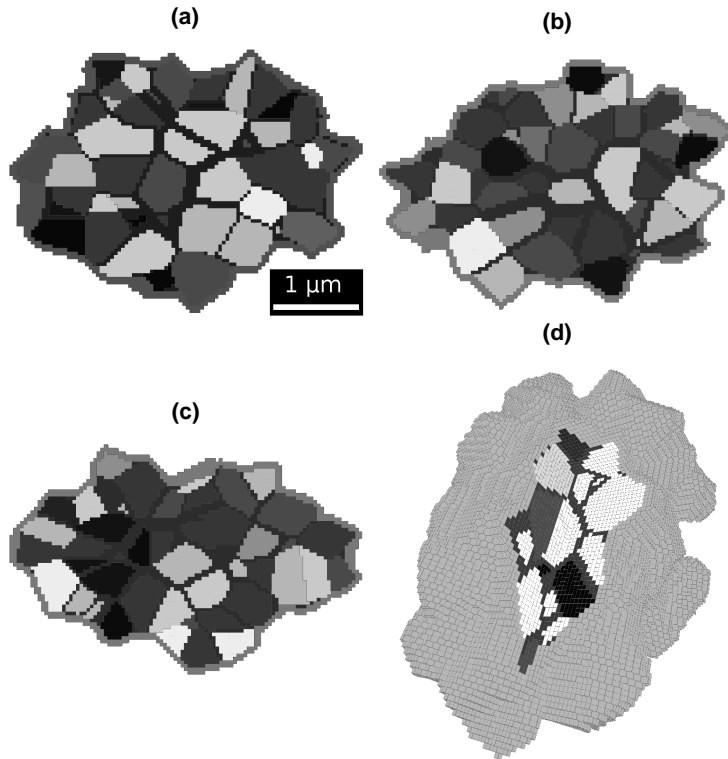


Figure 3. Example cross-sections of Case 1 versions of all three of the ensemble constituent particles (Panels **a–c**), and a three-dimensional rendering (Panel **d**) of the particle in Panel **(a)**, with a part of the particle cut out to reveal the inner structure. Different shades of gray correspond to different minerals. The scale bar in Panel **(a)** shows the approximate size of the features at the largest particle r used in this study, $1.75\ \mu\text{m}$.

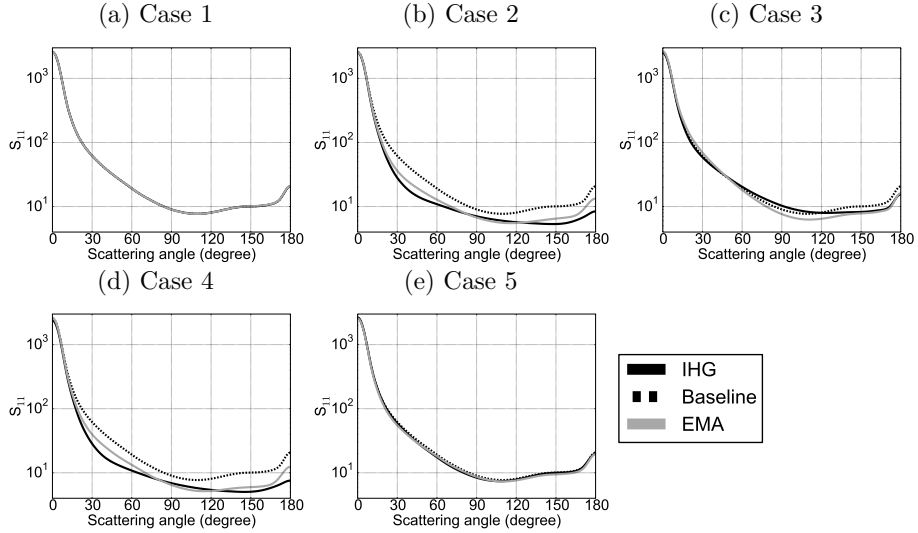


Figure 4. S_{11} values for the inhomogeneous (IHG), the baseline, and the homogeneous (EMA) versions of all five of the internal structure cases as a function of the scattering angle.

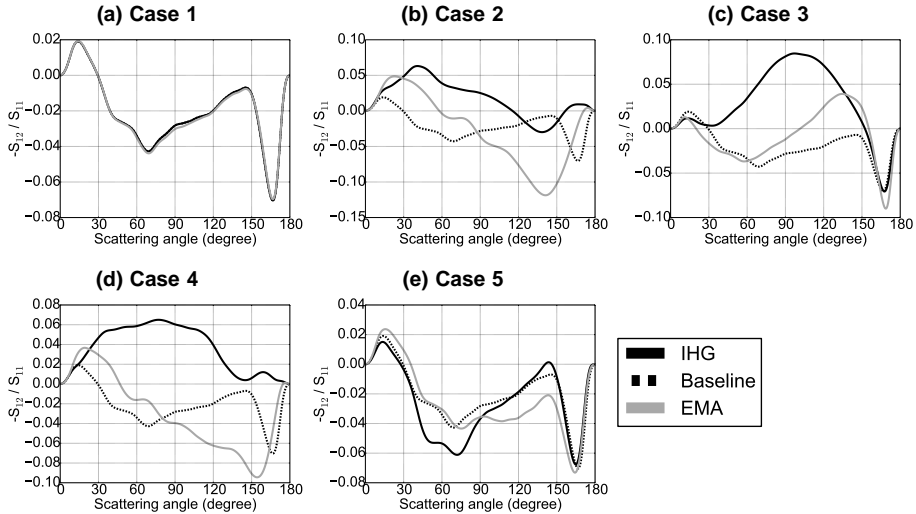


Figure 5. $-S_{12}/S_{11}$ values for the inhomogeneous (IHG), the baseline, and the homogeneous (EMA) versions of all five of the internal structure cases as a function of the scattering angle.

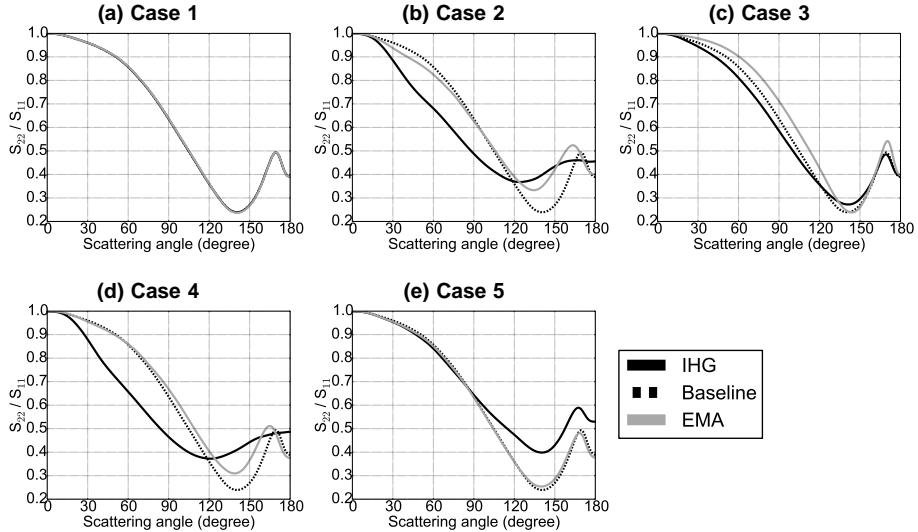


Figure 6. S_{22}/S_{11} values for the inhomogeneous (IHG), the baseline, and the homogeneous (EMA) versions of all five of the internal structure cases as a function of the scattering angle.

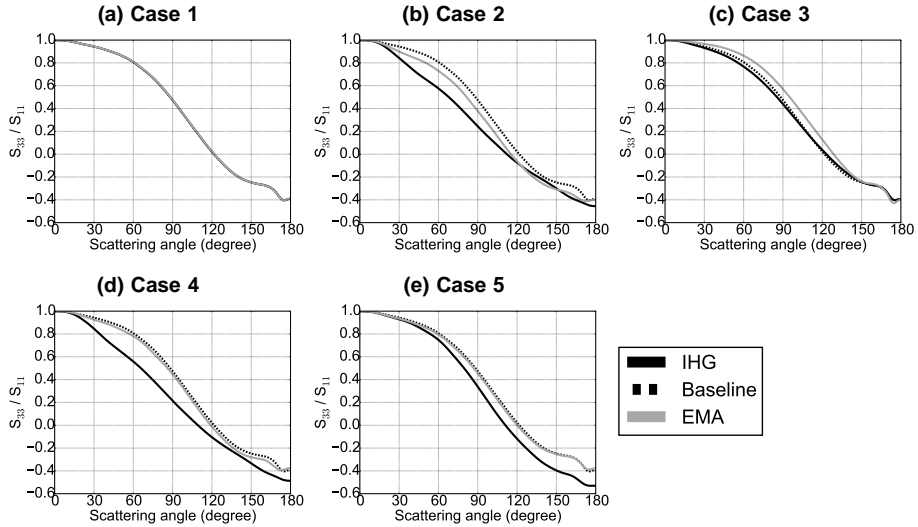


Figure 7. S_{33}/S_{11} values for the inhomogeneous (IHG), the baseline, and the homogeneous (EMA) versions of all five of the internal structure cases as a function of the scattering angle.

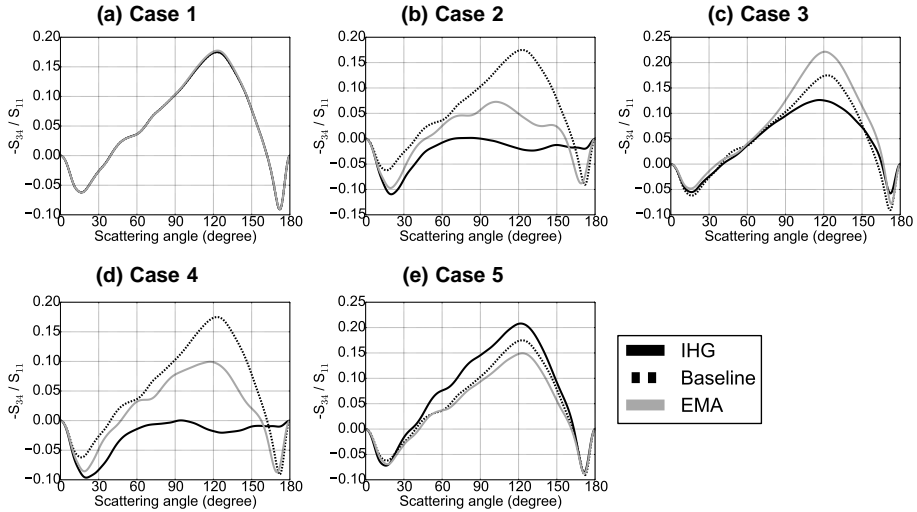


Figure 8. $-S_{34}/S_{11}$ values for the inhomogeneous (IHG) and the homogeneous (EMA) versions of all five of the internal structure cases as a function of the scattering angle.

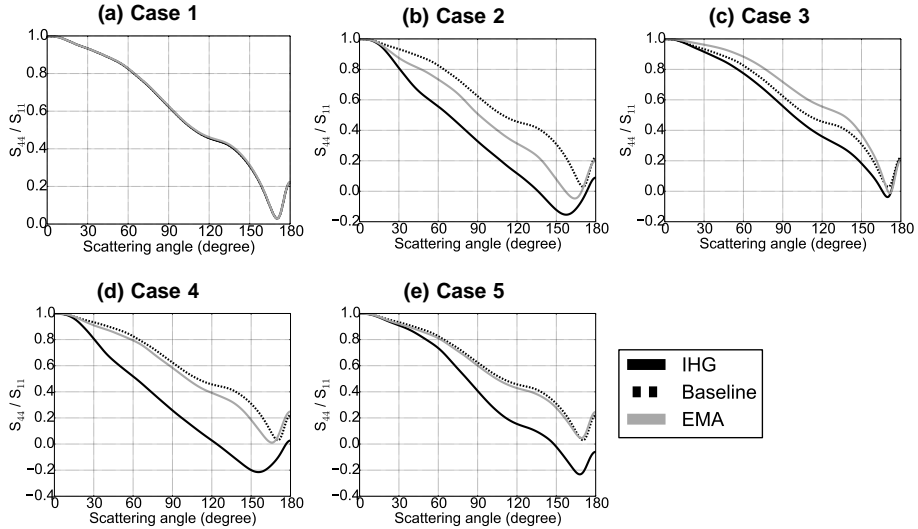


Figure 9. S_{44}/S_{11} values for the inhomogeneous (IHG), the baseline, and the homogeneous (EMA) versions of all five of the internal structure cases as a function of the scattering angle.

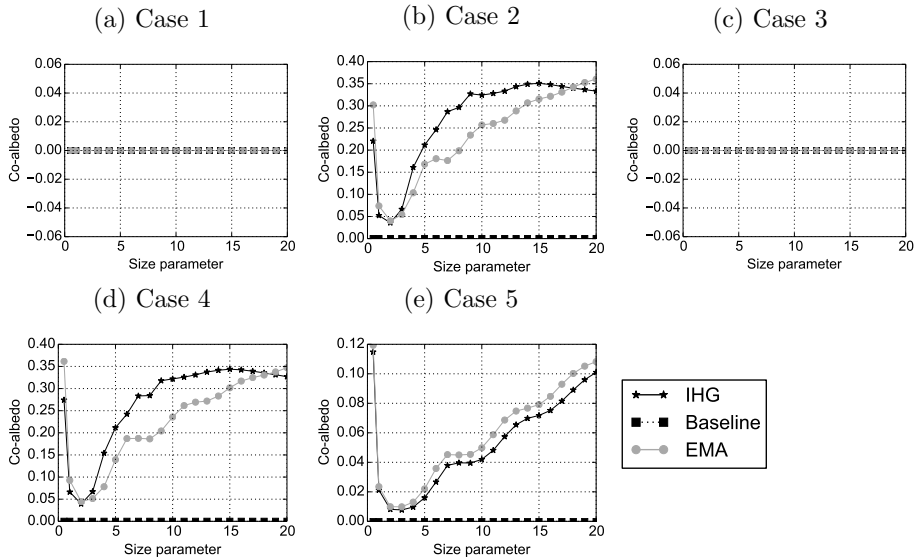


Figure 10. Albedo Co-albedo for the inhomogeneous (IHG), the baseline, and the homogeneous (EMA) versions of all five particle cases as a function of the size parameter of the particle.

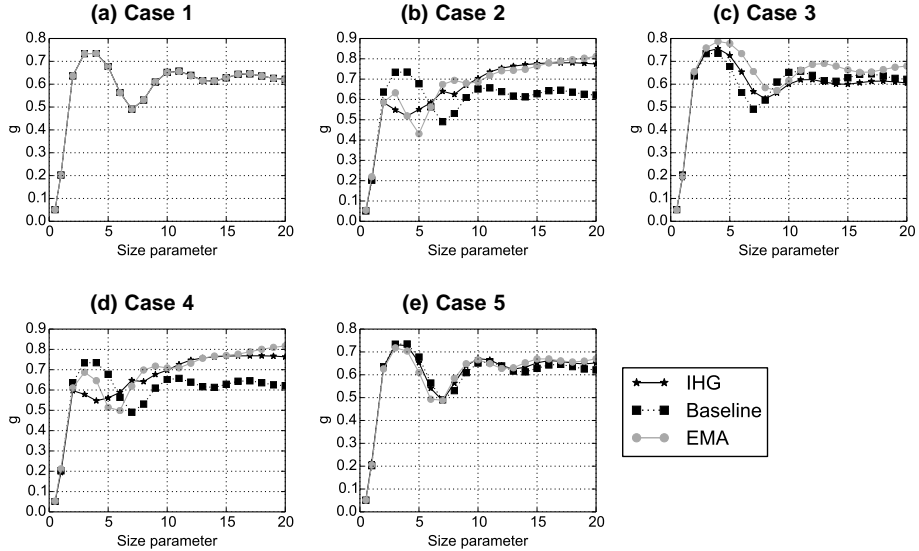


Figure 11. Asymmetry parameter for the inhomogeneous (IHG), the baseline, and the homogeneous (EMA) versions of all five particle cases as a function of the size parameter of the particle.

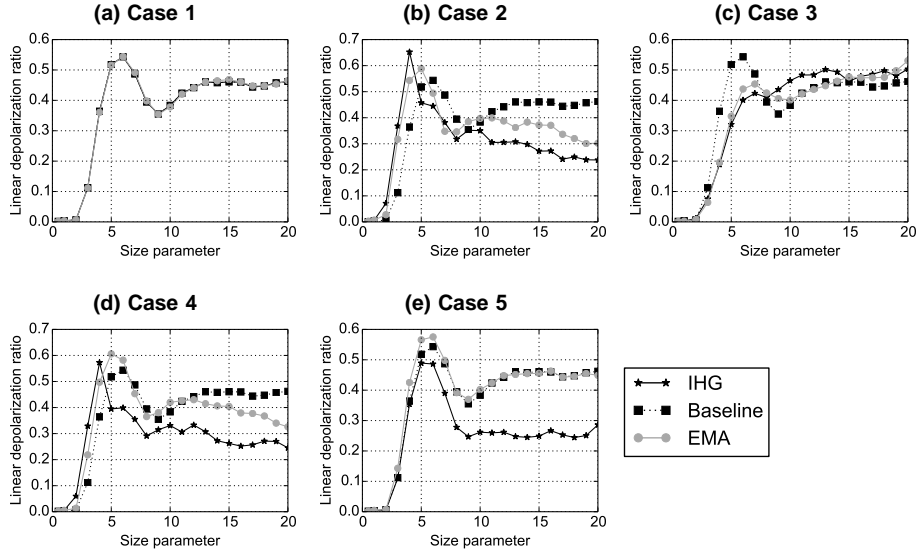


Figure 12. Linear depolarization ratio for the inhomogeneous (IHG), the baseline, and the homogeneous (EMA) versions of all five particle cases as a function of the size parameter of the particle.

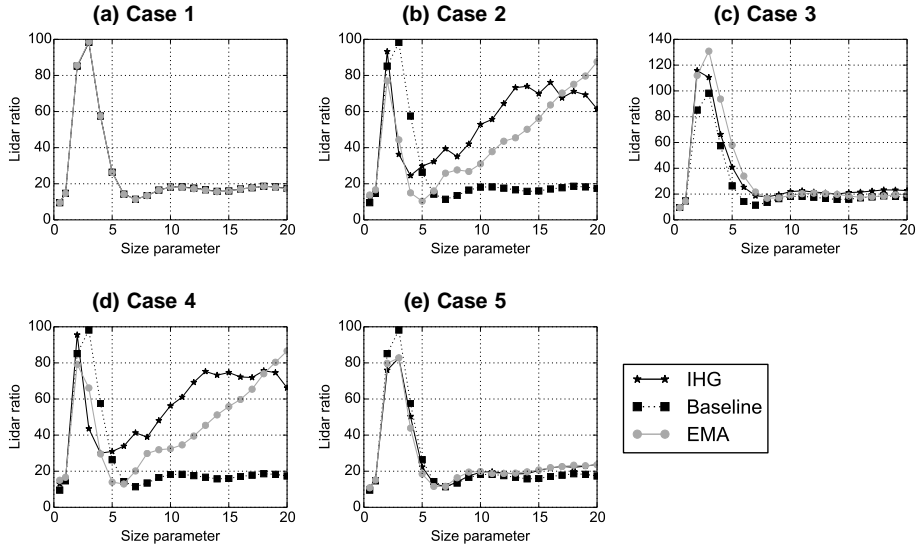


Figure 13. Lidar ratio for the inhomogeneous (IHG), the baseline, and the homogeneous (EMA) versions of all five particle cases as a function of the size parameter of the particle.